PROPOSAL TO CONSTRUCT AN ENDCAP ELECTROMAGNETIC CALORIMETER FOR SPIN PHYSICS AT STAR

W. Christie, T. Hallman, M. Schulz, K. Turner,
Brookhaven National Laboratory, Upton, N.Y. 11973, U.S.A.

G. Averichev, R. Badalian, S. Chernenko, L. Efimov, Y. Panebratsev,
E. Potrebenikova, D. Razin, S. Razin, O. Rogachevskiy, M. Tokarev, V. Yurevich,
Laboratory of High Energy Physics, JINR, 141 980 Dubna, Russia

J. Balewski, L.C. Bland, W.W. Jacobs, J.T. Londergan, J. Sowinski,
E.J. Stephenson, A. Szczepaniak, S.E. Vigdor*, S.W. Wissink,
Indiana University Cyclotron Facility, Bloomington, Indiana 47408, U.S.A.

B. Anderson, D. Keane, J. Watson, W. Zhang,
Kent State University, Kent, Ohio 44242, U.S.A.

A.M. Vander Molen, G. Westfall,
Michigan State University, East Lansing, Michigan 48824, U.S.A.

S. Heppelmann, A. Ogawa,
Pennsylvania State University, University Park, Pennsylvania 16802, U.S.A.

B.E. Bonner, G. Eppley, E. Platner, P. Yepes,
Rice University, Houston, Texas 77251, U.S.A.

V. Ghazikhanian, H. Huang, G.J. Igo, S. Trentalange, O. Tsai, C.A. Whitten Jr.,
UCLA, Los Angeles, California 90095, U.S.A.

G. W. Hoffmann, C. F. Moore, R. L. Ray, J. J. Schambach, H. J. Ward,
University of Texas, Austin, Texas 78712, U.S.A.

C. Pruneau and V. Rykov
Wayne State University, Detroit, Michigan 48201, U.S.A.

August 25, 1998

* contact person

Abstract

We propose the construction of a single endcap electromagnetic calorimeter (EEMC) for the STAR detector, to provide full azimuthal coverage over the pseudorapidity range $1.07 \leq \eta \leq 2.0$. Funds for the EEMC will be sought from the National Science Foundation, with some matching funds from Indiana University. The EEMC will add coverage crucial to the physics goals of much of the $\vec{\mathrm{p}} + \vec{\mathrm{p}}$ and p + A programs at RHIC. Most importantly, it will enable STAR to make the most definitive determination of the gluonic contribution to the proton's helicity of any experiment foreseen for the coming decade, via studies of the process $\vec{\mathrm{p}}\vec{\mathrm{p}} \rightarrow \gamma + \mathrm{jet} + X$ at $\sqrt{s}$=200 and 500 GeV. The endcap will further provide critical enhancements to other experiments probing the spin structure of nucleons and hyperons, unpolarized gluon distributions in nuclei, and manifestations of possible physics beyond the Standard Model in very hard $\vec{\mathrm{p}} + \vec{\mathrm{p}}$ collisions. In addition to the proposed EEMC design, we present detailed simulations for direct photon and for $\mathrm{W}^{\pm}$ production experiments, which impose the most stringent demands on detector performance, and therefore drive the design.

Contents

1 The Proposed Scientific Program

1.1 Overview

Studies of the structure of light hadrons present challenges unlike any faced previously in the science of matter at larger distance scales. In sharp contrast to the situation in molecules, atoms and nuclei, the mass of the nucleon originates *predominantly* in the *interactions* among its constituents, rather than in the "bare" masses of the constituents themselves. The strong color forces that confine quarks inside the nucleon lead to abundant gluons and sea quark-antiquark pairs. These gluons and sea quarks are then crucial "silent partners" in matter, making dominant contributions to the mass [1] of the visible world around us, without being manifested directly in the quantum numbers of the nucleon. Their "silent" contributions to mass have been modeled, successfully for many purposes, by subsuming them in phenomenologically determined effective masses of *constituent* quarks.

In order to make progress in understanding the structure of the nucleon, it is essential to probe the contributions of gluons and sea quarks to nucleon properties other than mass, and to see whether these, too, can be successfully modeled in terms of constituent quarks. Important contributions to the overall *spin* of a nucleon are expected, based on the results from a series of polarized deep inelastic scattering (DIS) experiments performed during the past decade [2, 3]. In these experiments, electromagnetic interactions are used to determine the combined spin structure functions of quarks and antiquarks in the nucleon. The results appear to suggest that quark and antiquark spins account for only $\sim$30% of the nucleon's spin, far less than expected from constituent quark models [4]. However, as discussed further below, the interpretation of the DIS results is ambiguous in the absence of independent information constraining the gluon spin contribution. The latter can only be probed by processes involving the *strong* interaction, and the prospects for interpretable measurements toward this end will be dramatically improved by the availability of colliding polarized proton beams at the Relativistic Heavy Ion Collider (RHIC), at energies where Quantum Chromodynamics (QCD) can be applied perturbatively to describe hard nucleon collisions.

The present proposal is aimed at construction of an endcap electromagnetic calorimeter (EEMC) for the STAR (Solenoidal Tracker At RHIC) detector, which will greatly improve its suitability for polarized proton collisions sensitive to gluon and sea quark contributions to the proton spin. The gluon contributions, in particular, affect hard quark-gluon or gluon-gluon collision processes, which lead to production of one or more hadron *jets*. The large acceptance of STAR makes it the instrument of choice at RHIC for jet detection. Addition to the baseline detector of a barrel electromagnetic calorimeter, already in progress, and of the EEMC proposed here, will facilitate a program of spin structure measurements complementary to that envisioned with the smaller-acceptance PHENIX detector at RHIC. The EEMC, in particular, is crucial for extending sensitivity to polarized partons carrying less than 10% of the proton's momentum, the region in which the vast majority of gluons and sea quarks reside.

The entire RHIC spin program is complementary to the heavy-ion collision experiments that are the central focus of RHIC: both aim to study the appropriate degrees of freedom for the description of hadronic systems, and especially the relationship of confined constituent quarks to the current quarks and gluons of QCD. The EEMC will support the heavy-ion collision program in other ways as well, for example, by facilitating measurements in (unpolarized) proton-nucleus collisions of the effect of nuclear matter on the distribution of gluons at low momentum fraction.

The latter measurements address another fundamental issue in nuclear physics, namely, the effect of surrounding nuclear matter on the structure of hadrons. The EEMC will also play a role in nucleus-nucleus collision studies, *e.g.*, by expanding the rapidity range over which one could search for anomalous ratios of neutral- to charged-pion multiplicities, one of the suggested signatures of the momentary restoration of the chiral symmetry of QCD in the very hot matter formed in RHIC collisions. Nonetheless, it is the spin program that drives the need and design for the EEMC, and we concentrate on that research in the following subsections.

1.2 Probing the Gluon Spin Distribution

The overall spin projection of a longitudinally polarized proton can be decomposed as follows:

$$S_z \;=\; \frac{1}{2} \;=\; \frac{1}{2}\Delta\Sigma \;+\; \Delta G \;+\; L_z^q \;+\; L_z^G, \tag{1}$$

where Σ represents the summed contribution from up, down and strange quarks and antiquarks, and G represents contributions from gluons. The Δ in each case denotes the integrated (over momentum fraction, as measured by Bjorken x) *difference* in parton distribution functions for parton spins aligned parallel *vs.* antiparallel to the proton spin; L_z denotes the net orbital angular momentum projection of the indicated partons. The results of polarized DIS experiments carried out at CERN, SLAC and DESY in recent years [3] are sometimes quoted as determining the value $\Delta\Sigma = 0.29 \pm 0.06$ (specified here [3] for a squared four-momentum transfer $Q^2 = 5\ \mathrm{GeV}^2$). This value is much smaller than that predicted (≈ 0.6) by relativistic constituent quark models [4]. However, the axial anomaly of QCD complicates the interpretation of the polarized DIS results [5], by introducing a dependence of the integrated asymmetry on ΔG, resulting in the *correlated* constraint on $\Delta\Sigma$ and ΔG shown in Fig. 1. (ΔG is actually a function of Q^2, but we suppress explicit mention of this dependence in most of what follows, for simplicity.) In fact, if ΔG were approximately +3, then not only $\Delta\Sigma$, but also the individual contributions from u, d and s quarks, would be restored to agreement with constituent quark models! Of course, then large and oppositely directed *orbital* contributions would be needed to reduce the overall proton spin projection to 1/2.

It is clear from these considerations that measurement of ΔG is the key to the next major breakthrough in understanding the nucleon's spin substructure. A precision better than ± 0.5 in ΔG would allow a meaningful assessment of the constituent quark model, by reducing the interpretation uncertainty for the DIS asymmetries to a level comparable to the present measurement uncertainties in these experiments. At present, ΔG is constrained only indirectly, by the spin-dependence of QCD-induced scaling violations in the DIS data [6], to lie roughly between zero and +3. The x-dependence $\Delta G(x)$ is essentially unconstrained, as suggested by the three very different "fits" in Fig. 2, where the gluon polarization $\Delta G(x)/G(x)$ near $x \approx 0.1$ varies from zero to 40%. Despite the fact that the gluon polarization for all three fits falls off with decreasing x, the integral $\Delta G \equiv \int_0^1 \Delta G(x) dx$ is still *dominated* in each case by contributions from $x < 0.1$, since this is the region where gluons are most abundant. [Note that $\Delta G(x)$ is multiplied by x in the curves in Fig. 2.] It is thus crucial to design measurements to constrain $\Delta G(x)$ to values of x as far below 0.1 as feasible.

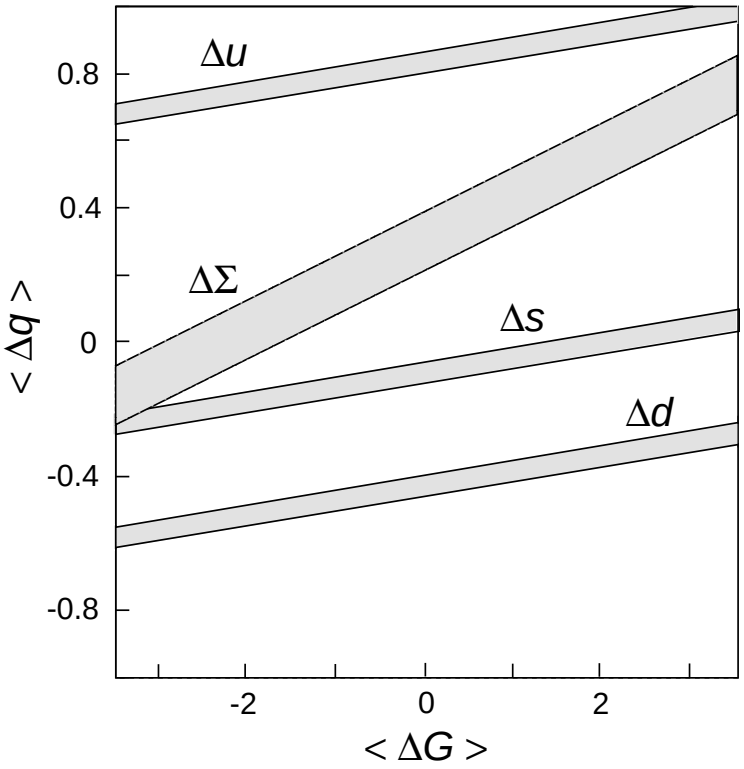

Figure 1: *The correlation of quark and gluon contributions to the longitudinal polarization of a proton, introduced by the effect of the QCD axial anomaly on the interpretation of polarized deep inelastic scattering asymmetries [3]. The separation of quark and gluon contributions to polarized DIS is scheme-dependent, and is shown here for one particular QCD factorization scheme. The bands in each case represent $\pm 1\sigma$ limits on the quark contributions deduced [3] from DIS results.*

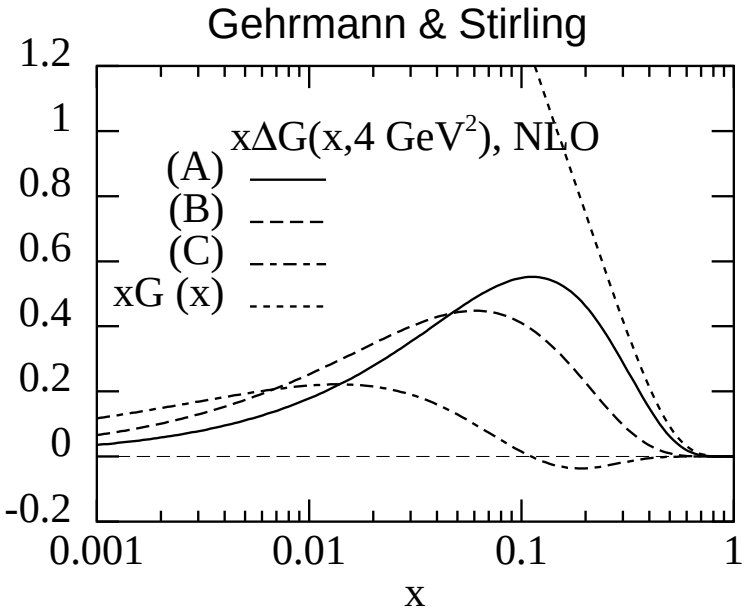

Figure 2: *Three models of the gluon helicity distribution used in next-leading-order global analyses of polarized DIS results by Gehrmann and Stirling [6]. All three are consistent with observed scaling violations in DIS. The solid curve (A) is used in simulations presented here.*

STAR measurements with the EEMC proposed here, of the processes $\vec{\mathrm{p}} + \vec{\mathrm{p}} \rightarrow \gamma$ + jet + X, jet + jet + X, would provide the best access to $\Delta G(x)$ at low x of any experiments contemplated at existing accelerators. Direct photon production in hard collisions (transverse momentum transfer $p_T \gtrsim 10$ GeV/c) is one of the most cleanly interpretable processes that can be studied in hadronic interactions [7]. Such high-p_T processes at RHIC energies ($\sqrt{s}$ = 50–500 GeV) are amenable to treatments in which the colliding proton beams are viewed as incoherent ensembles of parton beams – with luminosities and polarizations determined by the structure functions – participating in partonic collisions described well by low-order perturbative QCD. In the kinematic regions of greatest interest, photon production is dominated by a single partonic subprocess: quark-gluon Compton scattering, $q + g \rightarrow q + \gamma$. The main competing process, $q + \overline{q} \rightarrow \gamma + g$, contributes at the $\approx 10\%$ level. Direct photon events can be identified reasonably cleanly even by *singles* detection of the high-p_T photon. While such measurements have often been fitted to extract information [8, 9] on the *unpolarized* gluon distribution $G(x)$, they determine the relevant x-values only crudely, subject to an important ambiguity from the effect of transverse parton momenta ("k_T-smearing") in the initial state [8, 10]. Detection of the "away-side" jet (associated with the recoiling quark) in coincidence with the photon is necessary to determine the x-values of the colliding partons on an event-by-event basis, and thereby to extract the gluon distribution *directly* from the data. As will be explained later, the combination of coincidence measurements and polarization observables greatly reduces the sensitivity to k_T-smearing effects.

Inclusive jet or dijet production has the advantage over photon production of much larger cross sections, but the disadvantage of several competing partonic subprocesses, which are not all

equally useful in probing the gluon spin contribution. Furthermore, the resolution with which the colliding parton x-values can be determined is much cruder for dijet than for photon-jet coincidences. Nonetheless, the capability to measure *both* jet and photon production simultaneously with STAR adds a powerful internal consistency check on the extracted gluon helicity distribution $\Delta G(x)$. The electromagnetic calorimeters are necessary for energy measurements and triggering on photons and jets.

1.2.1 Direct Photon Production

The proposed EEMC expands the acceptance of the STAR detector for photons from the pseudorapidity range $|\eta| \leq 1.0$ to $-1.0 \leq \eta \leq 2.0$. For jets that are fully contained within the active volume, the increase is considerably more than a factor of two, from $|\eta| \lesssim 0.3$ to $-0.3 \lesssim \eta \lesssim 1.3$. But more importantly, the *endcap provides access to the phase space regions characterized by greatest sensitivity to ΔG and by cleanest extraction of x_{gluon} from the kinematics of the detected particles.* The importance of the endcap region is established by the following features of QCD and of the proton's spin structure:

1) QCD predicts large spin effects only when both colliding partons are polarized [11]. To measure the helicity preference of the gluons, one must study their collisions with partons that have substantial polarization of their own, preferably quarks at $x_{quark} \gtrsim 0.2$, where DIS results indicate quark polarizations in excess of 30%. Sensitivity to $x_{gluon} < 0.1$ is thus optimized for quite asymmetric quark-gluon collisions, where the partonic center-of-mass moves rapidly in the collider frame. Both products are then boosted toward the endcap.

2) Both the differential cross section and the partonic spin correlation $\hat{a}_{LL}$ for gluon Compton scattering peak strongly at backward c.m. angles θ^* [11], i.e., when the photon emerges in the same direction as the incident colliding quark: headed toward the endcap. These features combine with the steady increase in quark polarization as x_{quark} increases to give a figure of merit (FOM) characterizing the statistical sensitivity to gluon polarization that peaks well beyond $\eta = 1$. Although this argument has been based on Compton scattering in leading order, the same conclusion applies (the endcap's importance is even slightly *enhanced*) in calculations incorporating all contributions to the photon production in polarized proton collisions at next-to-leading order (NLO) [12].

3) The kinematics of photon-jet coincidences allow a clean event-by-event experimental determination of the momentum fractions $x_{1(2)}$ for the two colliding partons. However, an ambiguity remains concerning which x value corresponds to the gluon and, correspondingly, concerning the sign of $\cos\theta^*$. Both contributions must be included in fits of the data incorporating model gluon helicity distributions. One can still approach the ideal of a model-independent extraction of $\Delta G(x)$ most closely for the asymmetric collisions sampled by the endcap, where both the proton structure and the partonic differential cross sections strongly favor the assignment $x_{gluon} = \min[x_1, x_2]$. *No other proposed experimental method permits such a direct extraction of $\Delta G(x)$ from the measurements.*

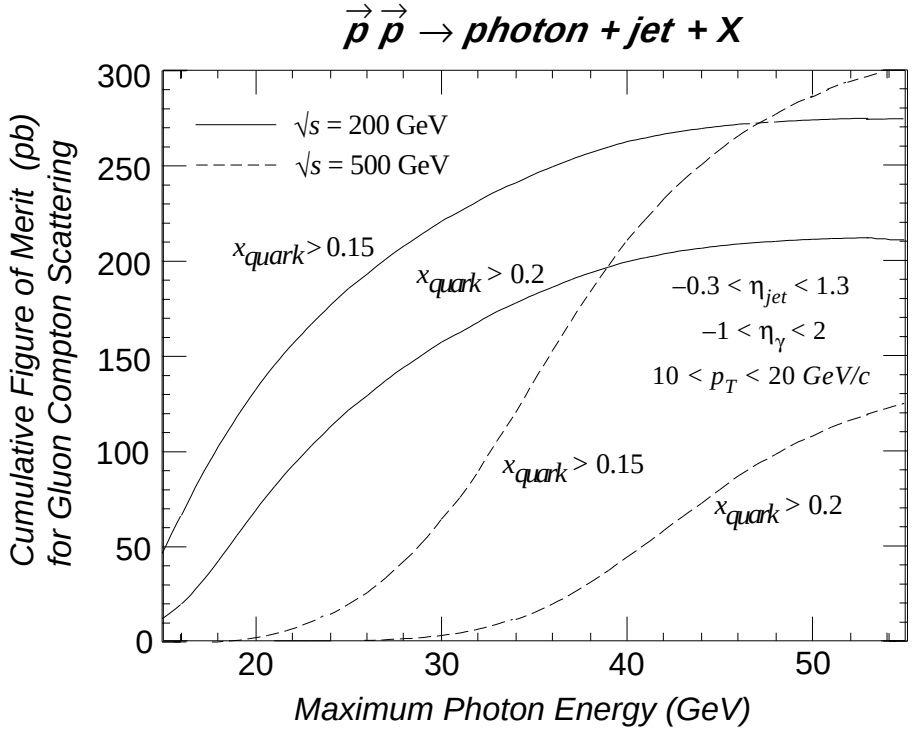

Figure 3: *The cumulative figure of merit (FOM) determining the statistical precision attainable in STAR measurements of gluon polarization via photon-jet coincidences, integrated over the full STAR acceptance, including the endcap calorimeter. The FOM is plotted as a function of the maximum photon energy one includes in the data sample. The FOM is determined from the differential cross section and spin correlation for the gluon Compton scattering process and the polarization of the colliding quark, assuming 100% polarized proton beams. Simulation results are plotted for two bombarding energies (neglecting the expected difference in luminosity between the two) and two lower cutoffs on the Bjorken x-value of the quark. The dominant sensitivity arises from (low x_{gluon}) events characterized by high-energy ($\gtrsim 20$ GeV) γ's detected in the proposed endcap EMC.*

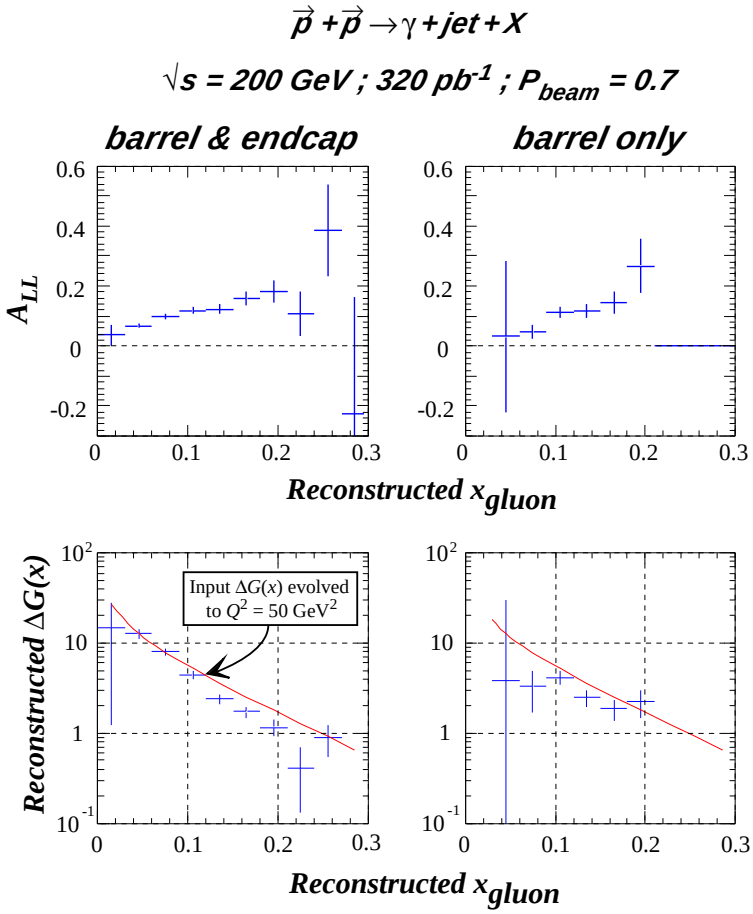

Figure 4: *Simulation results for the pp spin correlation A_{LL} and the gluon helicity distribution $\Delta G(x)$ extracted therefrom, for photon-jet coincidence events at $\sqrt{s}$=200 GeV. Simulations are shown for STAR with and without the proposed endcap EMC. The events analyzed have been subjected to cuts indicated in Fig. 15. The error bars reflect counting statistics for an integrated luminosity of 320 pb^{-1}. The solid curves in the lower frames represent the theoretical input for $\Delta G(x, Q^2 = 50 (GeV/c)^2)$. The systematic deviations between the input and extracted gluon helicity distributions arise from simplifying assumptions in the data analysis, and are correctable via simulations, as discussed in the text.*

The latter two points are illustrated, along with some of the demands on the EEMC and the quality of $\Delta G(x)$ data accessible, by simulation results in Figs. 3 and 4. In Fig. 3 we plot the FOM for gluon polarization measurements via $\vec{p}\vec{p} \rightarrow \gamma + \text{jet} + X$, *integrated* over the contributions from gluon Compton scattering events generated within the full STAR + EEMC acceptance, but only up to a maximum detected photon energy indicated on the abscissa. The contribution from each event is FOM $\propto \sigma(A_{LL}/P_{gluon})^2$, where σ and A_{LL} refer to the cross section and spin correlation for the pp system at the kinematics relevant to the given event; the gluon polarization P_{gluon}, which factors into A_{LL} (along with the partonic $\hat{a}_{LL}$ and P_{quark}), has been divided out to yield an effective analyzing power for the measurement of P_{gluon} itself. The quantity plotted thus represents an integrated statistical sensitivity of the measurements

to gluon polarization, as a function of the maximum photon energy at which we could cleanly distinguish γ's from π^0's in the calorimeter. The rapid rise observed in the figure indicates that determination of the integral ΔG places a very high premium on the clean detection of 20–50 GeV photons. Since the figure includes only events with *transverse* momentum $10 \leq p_T \leq 20$ GeV/c, these high energies reflect primarily photons falling in the endcap region. The need for clean $\gamma - \pi^0$ discrimination at such high energies is a central consideration in the EEMC design.

Figure 4 shows simulated STAR + EEMC results, for both the measured spin correlation $A_{LL}(x_{gluon})$ and the extracted $\Delta G(x_{gluon})$, attainable in a 10-week run at $\sqrt{s} = 200$ GeV. These are the results of more sophisticated simulations (described in more detail in Sec. 3 and in the Appendix), incorporating generation of all LO QCD processes for direct photon production, as well as initial-state gluon radiation and gluon splitting that introduce k_T-smearing, approximate Q^2-evolution of realistic structure functions, and event reconstruction and analysis algorithms (and assumptions) that would be applied to real data. The generated $\vec{\mathrm{p}} - \vec{\mathrm{p}}$ spin correlations in Fig. 4 decrease in magnitude with decreasing x_{gluon} because the gluon polarization input to the calculation (corresponding to the solid curve in Fig. 2) is falling. Nonetheless, the growing gluon abundance leads to a steady *increase* in the contributions to the integrated ΔG, as shown in the lower frame.

The $\Delta G(x)$ values *extracted* from the simulated events deviate systematically at $x_{gluon} > 0.1$ from the input distribution in Fig. 4 because the simple analysis performed neglects various effects included in the event generation. In particular, contributions from events where $x_{gluon} = \max[x_1, x_2]$ and from $q + \overline{q} \to g + \gamma$, both neglected in the analysis, act to dilute the measured $\vec{\mathrm{p}} - \vec{\mathrm{p}}$ asymmetries. The deviations also arise, in part, from the neglect in the analysis of the generated k_T-smearing and from reconstruction errors in θ^*, hence in the partonic $\hat{a}_{LL}$ values to use in extracting $\Delta G(x)$. Reliance on such simulations to correct for these deviations should introduce only a modest ($\sim 5\%$) model-dependence in the extracted integral ΔG, because the deviations are at worst $\sim 30\%$, and they become unimportant at $x_{gluon} < 0.1$, where one finds the dominant contributions to the integral.

That the endcap acceptance dominates the event sample at $x_{gluon} < 0.1$ can be seen from Fig. 5. For the majority of the asymmetric parton collisions that contribute here, the endcap is needed to detect *both* the photon and jet fragments. The endcap is also responsible for all of STAR's acceptance at $x_{gluon} > 0.2$, where at least part of the jet always falls beyond $\eta = 1.0$. Even in the middle region, $0.1 \leq x_{gluon} \leq 0.2$, the endcap leads to a reduction of statistical uncertainties by a typical factor ~ 2. Consequently, the quality of $\Delta G(x)$ information available from STAR *without* the EEMC is distinctly inferior, as also shown in Fig. 4. *The large improvement the EEMC gives in the quality of data at* $x_{gluon} < 0.1$ *is absolutely critical for constraining the extrapolation of* $\Delta G(x)$ *toward* $x = 0$*, and hence, to determining the integrated* ΔG *to the precision goal of* ± 0.5.

In fact, measurement of $\vec{\mathrm{p}}\vec{\mathrm{p}} \to \gamma + \mathrm{jet} + X$ at $\sqrt{s} = 200$ GeV alone is insufficient to constrain the $x \to 0$ extrapolation at the desired level. However, as detailed in the Appendix, an additional 10-week run at $\sqrt{s} = 500$ GeV would extend the covered x_{gluon} range down to ≈ 0.01, and reduce the extrapolation uncertainty to a level comparable to other expected systematic errors. The 500 GeV data may furthermore reduce the model-dependence associated with NLO corrections to the analysis, by allowing comparisons of results at common x_{gluon} values obtained at quite different momentum transfers.

The error bars in Fig. 4 include counting statistics only. These point-to-point relative error bars should be increased by an x-dependent factor of 1.5–2.0 to account for the estimated

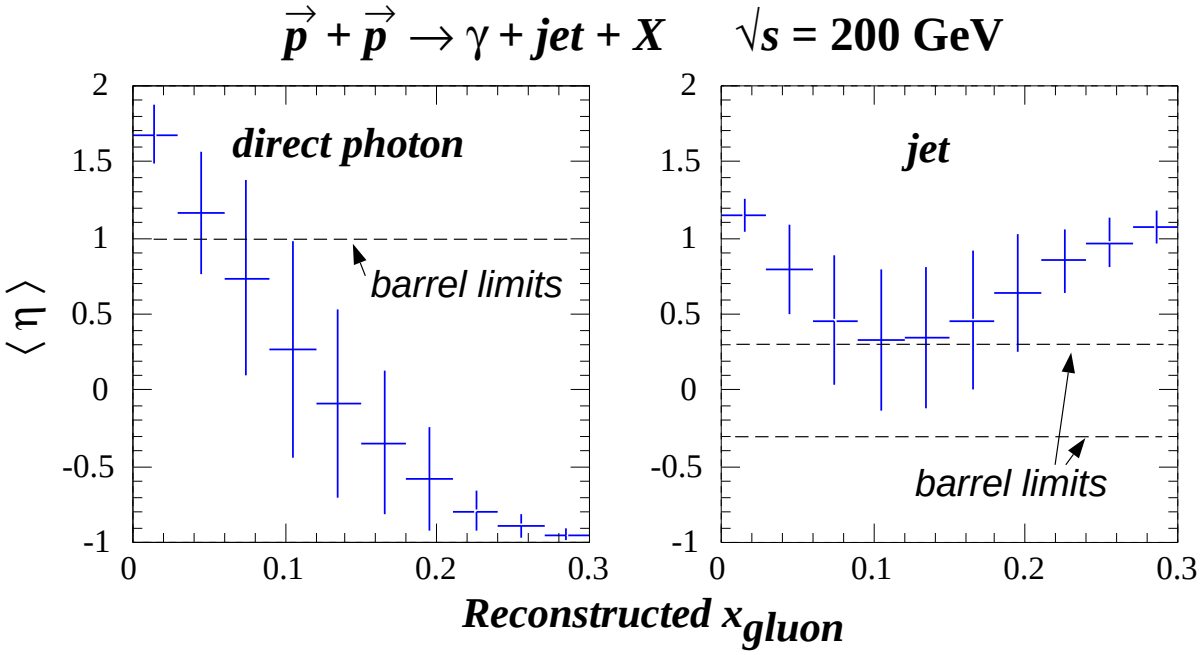

Figure 5: *Moments of the pseudorapidity distribution of simulated photon-jet coincidence events contributing to each bin in reconstructed x_{gluon} values in Fig. 4. Each point represents the mean contributing η-value for photons or jets, with the "error" bars reflecting the rms deviation from the mean. The dashed horizontal lines indicate the end of the barrel acceptance. These results demonstrate that the endcap dominates the acceptance for $x_g < 0.1$ and for $x_g > 0.2$, and is of substantial importance in the intermediate region.*

uncertainty (see Sec. 3.3) in subtracting background events where a π^0 or η^0 meson gets mistaken for a photon. Additional systematic relative errors can arise from false instrumental asymmetries. Assuming (conservatively) that these can be kept $\lesssim \pm 0.005$ in the measured $\vec{p} - \vec{p}$ asymmetries, their effect is negligible if the gluon polarization is, in fact, as large as assumed in the simulations for Fig. 4. However, for smaller gluon polarizations, including those relevant for 500 GeV measurements at $x_{gluon} < 0.05$, the instrumental asymmetries become significant. Combining 10-week runs at $\sqrt{s}$=200 GeV (320 pb^{-1}) and 500 GeV (800 pb^{-1}), the above contributions would yield an error $\approx \pm 0.2$ in ΔG integrated over the *measured* range $0.01 \leq x_{gluon} \leq 0.3$.

Additional appreciable systematic errors in the integrated ΔG will arise from uncertainties in the absolute proton beam polarizations, the DIS asymmetries used to determine the quark polarization, the *un*polarized distribution function $G(x)$, the EMC energy calibration upon which the reconstructed values of x_{gluon} are based, and corrections for simplifying assumptions made in the analysis (including neglect of NLO processes). The *full* integral ΔG will, of course, also be subject to systematic errors associated with the extrapolation to $x = 0$. The net systematic error resulting from these sources must be limited to $\approx \pm 15 - 20\%$ of the value of ΔG in order to reach the precision goal. This appears feasible, and places a premium on an eventual absolute calibration of RHIC beam polarizations to an accuracy of $\pm 5\%$.

1.2.2 Dijet Production

It is more difficult to extract $\Delta G(x)$ directly from *dijet* measurements, because both quark-gluon and gluon-gluon scattering processes contribute significantly [11], and it may be difficult to distinguish jets originating from quark *vs.* gluon fragmentation. Nonetheless, models of $\Delta G(x)$ can be tested by comparing their predictions to measured dijet asymmetries. Such measurements will be most useful in constraining structure function models if they span a sizable range in x_1 and x_2 values for the colliding partons and in partonic center-of-mass scattering angle, and hence in the expected *relative* contributions from qg *vs.* gg scattering.

The EEMC expands the STAR acceptance for such dijet coincidences very significantly. At $p_T \sim 10$ GeV/c, a jet is typically spread over a cone of half-angle (in pseudorapidity η and azimuthal angle ϕ) $\sqrt{(\Delta\phi)^2 + (\Delta\eta)^2} \approx 0.7$, and it is desirable that both jets be fully enclosed within the detector acceptance to avoid certain systematic errors in the kinematic reconstruction of the partonic collision. As in the case of the photon-jet coincidences, the coverage gained provides critical access to (1) asymmetric partonic collisions, which will enhance the relative contribution from quark-gluon scattering, and (2) forward partonic c.m. angles, where the parton scattering cross sections grow rapidly. Simulations show that the rate of dijet events with invariant mass above 20 GeV detected with STAR at $\sqrt{s}$=200 GeV grows by more than an order of magnitude when the EEMC is added.

1.2.3 Comparison to Other Techniques

Measurement of the gluon spin distribution is a high-priority focus of a few approved experiments, and is under discussion at other laboratories. The PHENIX collaboration at RHIC also aims to extract ΔG from direct photon detection in $\vec{p} - \vec{p}$ collisions [13]. However, their detector limits them to *singles* photon detection near mid-rapidity. The absence of kinematic reconstructions on an event-by-event basis permits only a crude determination of the relevant x_{gluon} values, based on a correlation with the measured p_T of the detected photon. The focus on mid-rapidity photons limits the minimum x_{gluon} value accessible to about twice that relevant for STAR with the endcap. Thus, although the two experiments have roughly comparable statistical precision goals, it is expected that the systematic errors associated with model-dependence in the analysis and with extrapolation toward $x_{gluon} = 0$ will be significantly larger for PHENIX. The PHENIX acceptance is too small to allow jet detection. It will be possible to look for mid-rapidity coincidences between photons and leading hadrons from jets, but in this case the resolution of the experimental reconstruction of parton x-values will be considerably worse than for detection of the full jet. As an alternative method for probing ΔG, the collaborators are considering the study of inclusive production of charmed or bottom mesons. However, the assumption that the hadroproduction mechanism is dominated by low-order gluon fusion processes is not very well supported by NLO calculations [14]. Furthermore, the experimental signature for the production is not very clear, since the detected daughter lepton carries only a small and highly varying fraction of the parent meson's momentum.

The approved COMPASS experiment [15] at CERN will use *lepto*production of open charm to measure $\Delta G/G$ averaged over the range $0.1 \lesssim x_{gluon} \lesssim 0.3$, in collisions of polarized muons with fixed polarized hydrogen and deuterium targets. A similar approach, with somewhat poorer sensitivity but an accelerated time schedule, is being considered by the HERMES collaboration at DESY. The statistical precision goal of COMPASS is roughly a factor of two coarser than that of STAR over the same x region. The additional access to lower x at STAR should, as explained

earlier, considerably heighten the physics impact of the result. While the leptoproduction mechanism seems under somewhat better control than that of hadroproduction of open charm, there still exist unexplained order-of-magnitude discrepancies between measured and predicted cross sections at relevant p_T values [16, 17].

Theoretically, the cleanest extraction of $\Delta G(x)/G(x)$ at low x_{gluon} could be made from scaling violations observed in polarized DIS, *if* the quality of data could be improved by an order of magnitude and extended over a much wider range of momentum transfer [6]. The acceleration of *polarized* proton, as well as electron, beams in the HERA collider at DESY might well facilitate the relevant measurements. However, any decision about pursuing this option will not be made before the year 2002.

In summary, among the contemplated experiments, STAR measurements with the EEMC in place have the greatest promise to yield definitive information on the integrated ΔG, via direct extraction of the x-dependent function $\Delta G(x)$, at a useful precision level. The theoretical uncertainties in analyzing STAR data are not negligible, as attested by continuing controversy [8, 9, 10] regarding the extraction of unpolarized gluon distributions from inclusive photon production. However, Vogelsang and Vogt [9] have estimated the theoretical uncertainties associated with ambiguous scale factors to be *minimized* in the x_{gluon} range of STAR. The largest ambiguities in the unpolarized analysis, associated with poorly constrained parton *transverse* momenta [8], appear from the simulations in Fig. 4 to have considerably smaller effects on the spin correlation asymmetries, for reasons elaborated further in Sec. 3.6.1. Furthermore, the availability of multiple bombarding energies and multiple detected reaction channels provides built-in tests of the theoretical uncertainties. There are also a number of crucial *experimental* concerns that must be addressed in the design of the EEMC, in the trigger electronics and in the analysis procedures, in order to ensure attainment of an optimized result. These are discussed, along with the proposed solutions, in Sec. 3.

1.3 Examples of Other Uses of the Endcap

1.3.1 Intermediate Vector Boson Production

Another important open question about nucleon structure concerns the contribution of sea quarks and antiquarks to the overall spin. The polarized DIS results, in the conventional interpretation (corresponding to assuming ΔG=0 in Fig. 1), suggest an appreciable helicity preference for strange sea quarks, *oppositely directed* to the proton's overall polarization. Is this conclusion valid, and if so, is the negative polarization shared by sea quarks and antiquarks alike, and by sea quarks of different flavor? Answers to these questions will contain clues to the physical origin of the sea, e.g., to the relative importance of processes in which virtual $q\overline{q}$ pairs are produced from gluons in the proton, as opposed to being associated with virtual π- or K-mesons – the Goldstone bosons which effect chiral-symmetry-breaking quark helicity reversals [18].

In the case of u and d quarks, sea contributions can be distinguished in experiments that probe *anti*quark polarization. The cleanest antiquark probes involve electroweak production of dilepton pairs (Drell-Yan processes) or of intermediate vector bosons ($W^{\pm}$, Z^0) in $\vec{p}-\vec{p}$ collisions. The $W^{\pm}$ production is of special interest because it is flavor-specific: the dominant partonic processes, $u+\overline{d}\rightarrow W^+$ and $d+\overline{u}\rightarrow W^-$, allow independent measurements of $\overline{d}$ and $\overline{u}$ polarization. Because the weak production is parity-violating, one can sample the parton polarizations via *single-spin* longitudinal analyzing powers [19]. In principle, then, it becomes possible to determine the relevant quark and antiquark polarizations *separately* from the same

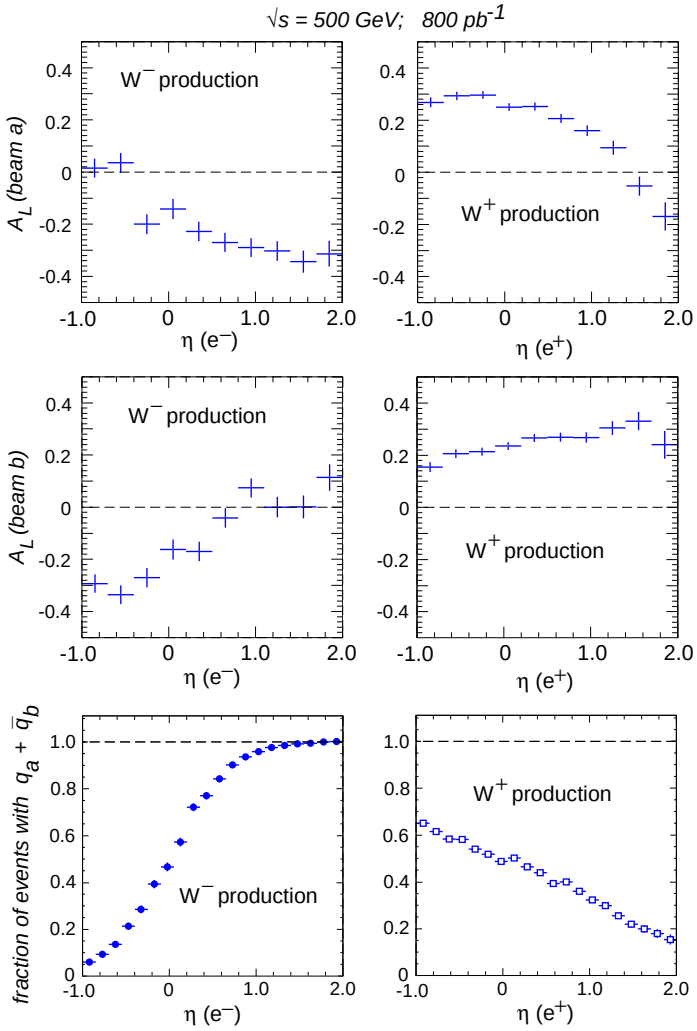

Figure 6: *Simulated single-spin parity-violating analyzing powers for W^- (left frames) and W^+ (right) production at $\sqrt{s} = 500$ GeV, plotted as a function of the pseudorapidity of the daughter $e^{\mp}$ detected in STAR + EEMC. The upper (middle) frames show the sensitivity to helicity flip of proton beam a (b) headed toward (away from) the endcap. The error bars reflect counting statistics only, for an integrated luminosity of 800 pb^{-1}. The lower frames show the fraction of simulated events within each η bin where the colliding quark comes from beam a and antiquark from beam b.*

data sample, by separately measuring the asymmetries associated with helicity reversal of one of the colliding beams or of the other. Where possible, this separation allows a powerful calibration of the analysis, by comparing the extracted quark polarization at, say, $x_{quark} \gtrsim 0.2$, to the values that are already very well constrained by DIS. Such a comparison can verify not only the method used to extract the poorly known *anti*quark polarizations, but also the continuing validity of the Standard Model for describing parity violation in weak processes at high p_T [11].

In practice, separation of the quark and antiquark polarization sensitivities works best for W^- production, and requires acceptance in the region of the endcap calorimeter. The $W^\pm$ production will be identified in STAR via detection of a high-p_T positron or electron from the W decay, in events characterized by large missing p_T (corresponding to an undetected daughter neutrino, see Sec. 3.4 for details on how missing p_T may be identified in a non-hermetic detector). The $e^{-(+)}$ are emitted preferentially parallel (antiparallel) to the left-handed $W^{-(+)}$ momentum direction. Hence, electrons detected in the endcap preferentially sample W^- produced in asymmetric $d\overline{u}$ collisions, which move toward the endcap themselves. In this kinematic regime, the structure functions strongly favor assignment of the d quark (at relatively high x) to the beam proton headed toward the endcap and of the (low-x) $\overline{u}$ to the other proton. Indeed, the simulations in Fig. 6 (for $\sqrt{s} = 500$ GeV) show that this assignment is correct for 98% of the W^- decay electrons detected in the endcap, in marked contrast to the much more balanced contributions from the two possible assignments in the W^+ case. Figure 6 also indicates the statistical precisions attainable for the various parity-violating asymmetries with STAR + EEMC, and the values expected for one particular choice of spin-dependent quark and antiquark distribution functions [6] (see also Refs. [19, 20]).

Measurements of $W^\pm$ production require good electron-hadron discrimination with STAR. It will be shown in Sec. 3.4 that the expected performance is suitable. On the other hand, clean distinction of W^+ from W^- events will become problematic for $\eta > 1.5$, where STAR's time projection chamber (TPC) provides very limited resolution to discern the sign of the curvature of the very rigid $e^\pm$ tracks of interest. This issue is discussed further in Sec. 3.5.

1.3.2 Searches for Physics Beyond the Standard Model

The capability to measure parity-violating asymmetries in very hard partonic collisions with STAR provides an opportunity to perform unique and important tests of the Standard Model. For example, the Standard Model predicts [11, 21, 22] parity-violating two-spin asymmetries (i.e., a sensitivity of the cross section to the simultaneous flip of both beam helicities) for inclusive jet production reaching several percent at $p_T \sim 100$ GeV/c. This effect arises, for example, from the interference of quark-quark interactions mediated by gluon- *vs.* Z^0-exchange. However, such hard collisions may also be sensitive to interference with amplitudes associated with new phenomena at a mass scale ~ 1 TeV. As one example, a new ultra-short-range interaction associated with quark *compositeness* might well violate parity [11, 22]. Modifications to the Standard Model predictions might similarly arise from the exchange of new heavy gauge bosons, such as proposed in [23]. Searches for such new phenomena will constitute an important goal of second-generation STAR spin experiments, after one first learns how to approach the requisite precision (statistical plus systematic uncertainties $\lesssim \pm 0.01$) for asymmetries measured at much smaller momentum transfer. The endcap EMC will be an important addition for any such searches, by virtue of its considerable expansion of the acceptance for jets.

1.3.3 Single-Spin Transverse Asymmetries

Sensitivity of the partonic processes to *transverse* polarization of one of the colliding beams is not prohibited by parity conservation, as in the case of longitudinal polarization, but is rather suppressed by the chiral symmetry of QCD [24]. The mass terms in the QCD Lagrangian explicitly violate chiral symmetry, and can give transverse spin analyzing powers (A_T) of order m_q/p_T. For hard processes involving light quarks at RHIC energies, one expects vanishingly small A_T in leading-order perturbative QCD. It is important, at an early stage in the RHIC spin program, to test the assumed validity of perturbative QCD in the kinematic regimes of interest for the experiments described above, by measuring A_T for at least some of the processes considered. These measurements involve similar detection issues, and the same needs for the EEMC, as discussed for extraction of parton helicity distributions.

1.3.4 Quark Transversity Distributions in the Proton

Even if all the parton helicity distributions could be mapped out, we would still not have a complete picture of the nucleon's spin substructure. New and independent information is contained in the *transversity* distributions $\delta q(x, Q^2)$, which measure the difference in probabilities for finding quarks with spin orientation parallel *vs.* antiparallel to the spin of a *transversely* polarized nucleon [25, 26]. (There can be no transversity for the spin-one gluon). When expressed in a helicity basis, $\delta q(x, Q^2)$ is related to the probability of helicity flip between the emission of a quark by the nucleon and the reabsorption of a quark by the nucleon. It is expected to differ from the helicity distribution $\Delta q(x, Q^2)$ by virtue of the relativistic behavior of the quarks in the nucleon. The availability of transversely polarized proton beams at RHIC raises several possibilities for probing these so far unknown structure functions in leading-twist processes. Among the suggested approaches [26] for which STAR is particularly well suited are: transverse spin correlations (A_{TT}) in $\vec{\mathrm{p}}_\perp\vec{\mathrm{p}}_\perp \to Z^0X \to e^+e^-X$; comparison of A_{TT} to A_{LL} for inclusive jet or dijet production; measurement of three-fold correlations of the form $(\vec{k}_{\pi^+} \times \vec{k}_{\pi^-}) \cdot \vec{S}_\mathrm{p}$ in the process $\mathrm{p}\vec{\mathrm{p}}_\perp \to \mathrm{jet} + X \to \pi^+\pi^-X$, with one transversely polarized beam and fragmentation pion pairs near the ρ-meson in invariant mass [27]. Each method has difficulties [26], not least of which is that it probes the product of a quark transversity function with another as yet unknown distribution. In any case, however, the addition of the endcap, by significantly expanding coverage for Z^0 and dijet events, places STAR in a good position to contribute meaningfully to transversity measurements as the subject matures.

1.3.5 The Unpolarized Gluon Distribution in Nuclei

Simulations of the early stage of ultra-relativistic nucleus-nucleus collisions indicate that gluons at low Bjorken x make the dominant contributions to the energy density of the system produced at mid-rapidity, and thus have strong influence on predicted signatures of the transition to a quark-gluon plasma (QGP) [28]. At the relevant x-values, the (unpolarized) distribution of gluons inside a nucleus may be strongly affected by "shadowing" [29]. The extent of shadowing must be measured in order to remove substantial ambiguities in present theoretical predictions of QGP signatures. Some information on the gluon structure function in nuclei is provided by the NMC experiment at CERN and by Fermilab experiments E665, E706, E772 and E789. However, the available data in the region of greatest interest ($0.01 < x_g < 0.05$) tends to be limited either by systematic errors or by low statistics.

STAR with the endcap EMC can measure the relevant gluon densities via direct photon and jet production in unpolarized p + A collisions. It is most desirable to use the well understood quark distributions in the proton at $x_q > 0.1$ to probe the low-x gluons in the nucleus. Just as described above for the p-p case, the acceptance for such asymmetric partonic collisions relies primarily on detection of energetic photons or jets (at least in part) in the endcap. The results will have intrinsic interest in testing our understanding of partonic interactions in nuclear matter, and will provide essential support for the interpretation of nucleus-nucleus collision data obtained at RHIC.

1.3.6 Polarized Gluon Distribution in the Neutron

It would clearly be of great interest to complement the measurements of gluon and anti-quark helicity preferences in a longitudinally polarized proton with similar measurements for a polarized neutron. Such measurements may be feasible in a second generation of STAR spin experiments, if polarized ^{3}He beams can be successfully produced and accelerated at RHIC. Polarized deuteron beams would be difficult to handle, because the small magnetic moment demands unreasonably strong Siberian Snakes and spin rotators. However, the ^{3}He option appears to be a promising path for a future upgrade. The effects of depolarizing resonances for ^{3}He beams are currently being evaluated [30]. The maximum energy attainable for ^{3}He, ≈ 160 GeV/nucleon, would limit the feasibility of W production experiments, but would be quite suitable for direct photon production.

1.3.7 Spin-Dependent Fragmentation Functions in Hyperon Production

Tests of models of spin substructure can be extended, in principle, beyond nucleons to short-lived hadrons, if one can measure the polarization of such hadrons when they appear as substantial fragments of a partonic jet. The case considered most extensively to date [31] is that of the Λ hyperon, whose weak parity-violating decay provides a self-analysis of the Λ's polarization. By measuring the polarization transfer at RHIC from one longitudinally polarized proton beam to Λ's produced inclusively at high p_T, one gains sensitivity to the *polarized fragmentation functions* for the Λ [31]. These functions measure the difference in probabilities for a parton of given helicity to fragment into a Λ of the same *vs.* opposite helicity. The functions depend on the flavor and mass scale of the final-state parton, and on the fraction z of the parton's momentum carried by the Λ. As pointed out recently by de Florian *et al.* [31], existing LEP data on fragmentation into polarized Λ's provide very little constraint on the flavor-dependence of the polarized fragmentation functions, whereas RHIC measurements for the inclusive process $\vec{\mathrm{p}}\mathrm{p} \to \vec{\Lambda} X$ at $\sqrt{s} = 200$ or 500 GeV could distinguish clearly among possible scenarios. RHIC data for Λ spin-dependent fragmentation could thus elucidate whether the nucleon "spin puzzle" has an analog in the hyperon sector as well [32].

The STAR detector with the proposed EEMC is well suited for the relevant measurements. The pseudorapidity range $\eta_\Lambda \gtrsim 1$ yields the greatest sensitivity to the polarized fragmentation functions [31], simply because this region emphasizes asymmetric parton collisions where the polarized proton beam headed toward the endcap is most likely to contribute a highly polarized (valence) quark. The endcap is needed to trigger on high-p_T jets in this region, while the TPC will permit reconstruction of the Λ (and direct measurement of its longitudinal polarization and of its jet momentum fraction z) from its daughter proton and π^- tracks. At $p_T \sim 10$

GeV/c and $\eta \lesssim 1.5$, there is a high probability that the Λ will decay well within the active TPC volume. The EEMC would also serve another purpose important to the interpretation of the results: by providing detection of correlated few-GeV γ's and π^0's, it could be used to tag those Λ's that result from the decay of heavier hyperons ($\Sigma^0 \to \Lambda\gamma$ or $\Xi^0 \to \Lambda\pi^0$), as distinguished from the Λ's that are direct fragmentation products. These different samples are likely to have quite different spin-dependent fragmentation functions, because the parton spin coupling in the heavier hyperons is expected to differ dramatically from that within the Λ. For a similar reason, it would be interesting to compare the Λ results to polarized fragmentation functions for Σ^+, which could be detected via its decay to $p\pi^0$.

2 Design of the EEMC

2.1 Overview of the STAR Detector

The Solenoidal Tracker At RHIC (STAR) has a geometry similar to many high energy detectors, in the sense that it attempts to enclose the full solid angle around the interaction point with detectors. The STAR detector components, sensitive to both hadrons and electromagnetic particles, are housed inside a cylindrically symmetric room temperature solenoidal magnet, as shown in the quarter section of Fig. 7. The detector is designed to track many charged particles simultaneously through the 0.5 T solenoidal field, to reconstruct jets, and to perform calorimetry on electrons, photons and electromagnetically decaying neutral mesons.

The heart of the detector is a time projection chamber (TPC) which provides tracking and momentum analysis information over the nominal pseudorapidity range $-2 \leq \eta \leq +2$ (15.4° to 164.6°). These momentum measurements are used to determine charged hadron energies. Electromagnetic energy is measured primarily by calorimetry. The Barrel Electromagnetic Calorimeter (BEMC) is a Pb/scintillator sampling calorimeter $\sim$18 radiation lengths deep and covers $-1 \leq \eta \leq +1$. It is the last detector layer before the magnet coils and includes a shower maximum detector (SMD) of high position resolution for γ/π^0 separation and e/hadron separation. Additional tracking and vertex detection is provided by a silicon vertex tracker (SVT) placed immediately around the beam pipe. A scintillator barrel, the Central Trigger Barrel (CTB) located just outside the TPC and covering -1$\leq \eta \leq$1, is used for triggering. After a planned upgrade, the latter will also provide high-resolution time-of-flight information for improved hadron particle identification. Additional triggering capability on charged particle multiplicities in the $1 \leq absη \leq 2$ region is provided by the multiwire chambers (MWC) in the end planes of the TPC.

Currently unfunded is electromagnetic calorimetry in the region $1 \leq |\eta| \leq 2$, i.e., covering the poletips to close the cylinder at both ends. This section of the proposal describes a conceptual design for an Endcap Electromagnetic Calorimeter (EEMC) to cover one pole tip. Driven by the p-A program, our intention is to install the proposed endcap EMC on the west poletip of the STAR detector: other detector and machine configurations already fixed at RHIC dictate that the proton beam in p-A collisions will be headed in the westerly direction at STAR. With the addition of this EEMC to STAR, the solid angle for jet reconstruction is greatly enhanced and most importantly, critical coverage is provided for the electromagnetic channels important to the physics goals of the STAR spin and p+A programs.

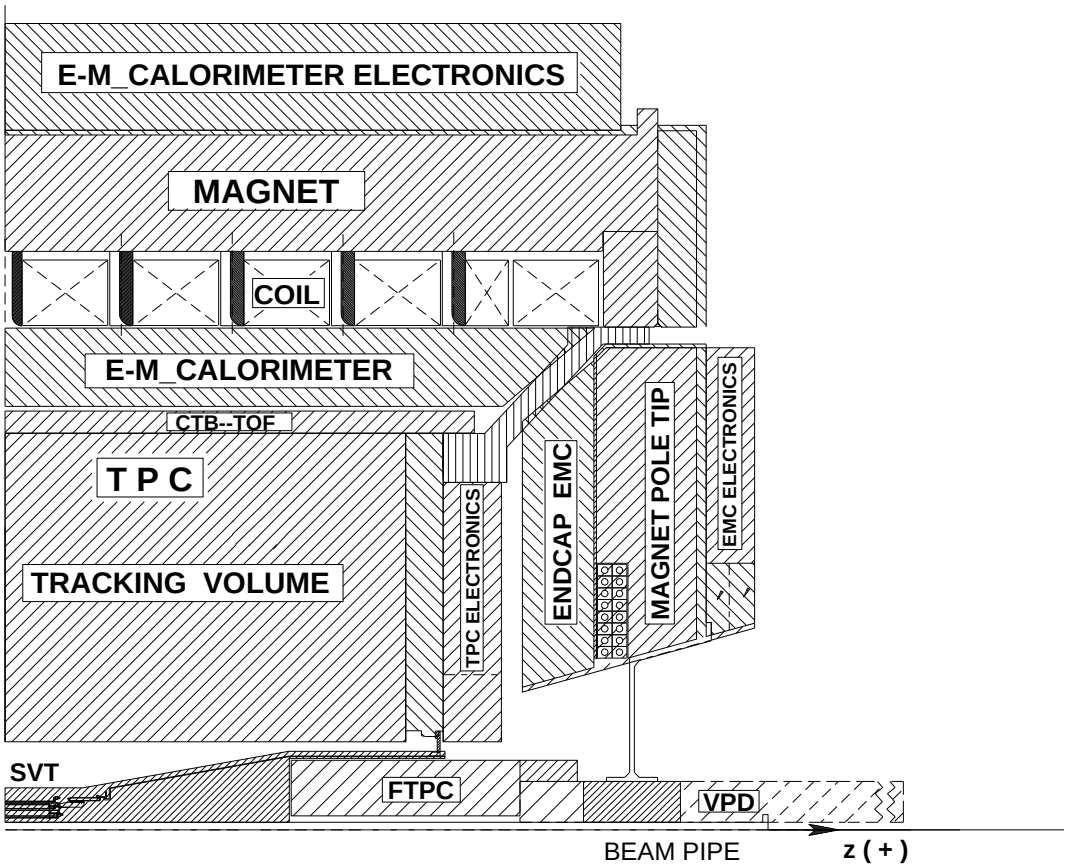

Figure 7: *A quarter-section of the cylindrically symmetric STAR detector, showing where the proposed endcap EMC would fit. Also indicated are the time projection chamber (TPC), central trigger barrel (CTB), barrel EMC, silicon vertex tracker (SVT), forward TPC (FTPC) and a projected vertex position detector (VPD).*

2.2 Endcap Calorimeter Design Considerations and Summary

The endcap calorimeter must have the following basic properties to meet the physics goals outlined in this proposal. It must cover the forward solid angle as fully as possible for $1 \lesssim \eta \leq 2$, within the space constraints imposed by the rest of the STAR detector. It must be thick enough to measure the energy of electrons and photons over a wide dynamic range, from < 1 GeV to $>$ 100 GeV, with good resolution and a high degree of linearity. The segmentation must be sufficient to allow clean triggering on isolated high-energy photons or electrons, and to avoid significant multiple particle occupancy of the finest segments in $p - p$ and $p - A$ collisions. The physics demands place a high premium on γ *vs.* π^0 and electron *vs.* hadron discrimination. The detector response must be fast enough to permit easy distinction of particles arriving from different beam crossings (110 ns apart at RHIC). And the EEMC should provide position information for electrons and positrons with sufficient resolution to permit unambiguous matching to the corresponding charged-particle tracks in the TPC, even in the presence of background TPC tracks from hundreds of neighboring beam crossings (see Sec. 3).

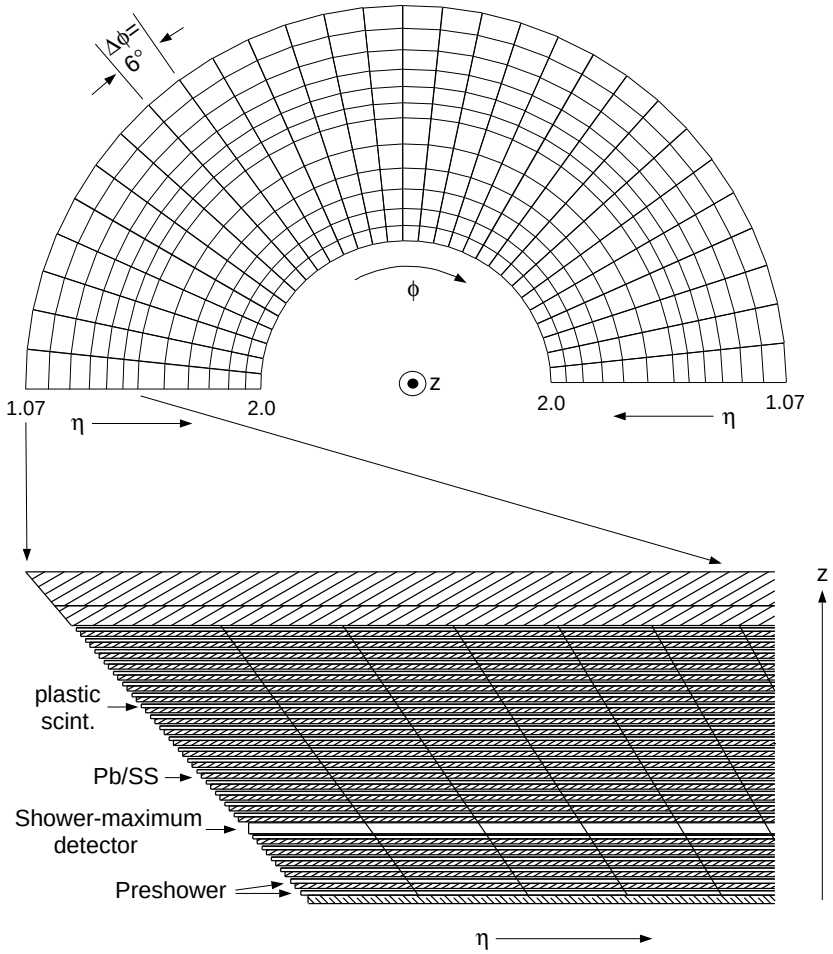

Figure 8: *Proposed tower structure of the EEMC. Frame (a) shows the subdivision (into a total of 720 towers, half of which are shown) in pseudorapidity and azimuthal angle. Frame (b) indicates the depth profile of the projective towers, each with 23 layers of lead/stainless steel absorber and plastic scintillator. The space left for the shower-maximum detector (SMD) is indicated.*

We have chosen a traditional Pb sampling calorimeter for the EEMC design, with the geometry illustrated in Fig. 8. Twenty-three layers of lead and twenty-four layers of plastic scintillator, arranged in an alternating pattern, give a total depth of 21 radiation lengths ($21X_0$), sufficient to provide energy resolution $(\Delta E/E)^2 \approx (16\%/\sqrt{E})^2 + (2\%)^2$ up to >100 GeV. Neglecting non-normal incidence (i.e., essentially for $\eta \to \infty$), the average energy leakage out the back of the endcap would be about 2% for 30 GeV photons and about 9% for 150 GeV electrons. Clearly, the non-normal incidence helps a bit in this regard. The stochastic term (2%) in the energy resolution is determined from fitting our simulation results, and is quite consistent with performance of other analogous calorimeters.

The calorimeter volume is divided into 720 projective towers, ensuring low occupancy for the tens of products expected for typical $p-p$ and $p-A$ collisions. The light output from each of the 24 scintillator layers within each tower is routed via optical fibers to a common

photomultiplier tube mounted outside the magnet. The first two scintillator layers are also read out separately, through additional fibers, as a "preshower" detector to help distinguish electrons from hadrons and γ's from π^0's, via differences in their initial shower development. The absorbing layers comprise 4.7-mm thick Pb sheets clad with stainless steel. The scintillator tiles are each 4 mm in thickness, with the exception of the preshower layers, where the thickness is increased to 5 mm to compensate for the sharing of light output between two optical fibers. There is on average $\approx$1 radiation length of material associated with the TPC in front of the calorimeter. A highly segmented "state-of the art" scintillator hodoscope consisting of 2 crossed planes (depicted in Fig. 9 and described in detail below) is placed near the depth of maximum shower development to provide fine position resolution, needed especially to resolve the two close-lying photon showers characterizing π^0 and η^0 decay.

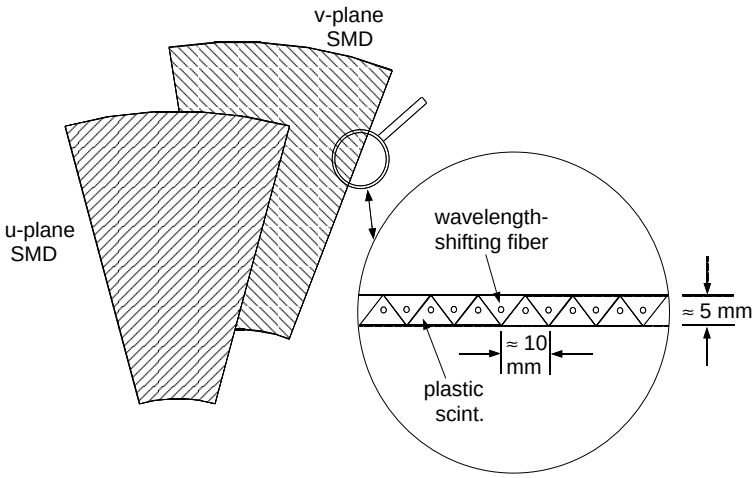

Figure 9: *Schematic layout of one 30° sector of the proposed SMD. Each of the two orthogonal planes will be constructed from triangular scintillating strips extruded with an axial hole for the wavelength-shifting fiber.*

The endcap is an annulus of approximate inner radius $\approx$75 cm, outer radius $\approx$215 cm and depth $\approx$33 cm. The inner and outer radii grow with depth, as indicated in Fig. 7, to define constant pseudorapidity. The actual range covered is $1.07 \leq \eta \leq 2.0$, leaving a small gap between the endcap and barrel calorimeter, needed for services to exit the solenoid. (Simulations indicate that this gap necessitates small corrections to measured jet properties, but does not compromise the physics goals of this proposal.) The full annulus will be divided into two halves for ease of assembly and transport, with each half segmented as shown in Fig. 8. Each of the towers mentioned above spans approximately 0.1 unit in azimuthal angle ϕ and either 0.05 or 0.1 unit in η. The change in η segmentation is made to maintain a manageable minimum transverse dimension for each scintillator tile, a number that is driven by the minimum bend radius (3 cm) of the readout fibers, and one which strongly influences the transverse shower leakage at maximum η. For example, $\sim$ 95% of the energy deposition for 30 GeV photons at the 5^{th} layer is contained within a cone of radius 2.0 cm. This means that the majority of showers near maximum η will be shared among two or more towers. On the other hand, the gaps between adjacent towers in our design is minimal, and the SMD does not follow the tower geometry, but

is arranged in 30° sectors, and should clearly indicate the centroid of shared showers. A cross section showing the layout of the towers *vs.* depth is also shown in Fig. 8.

Details of the EEMC conceptual design, as presently envisioned, are provided in the following sections.

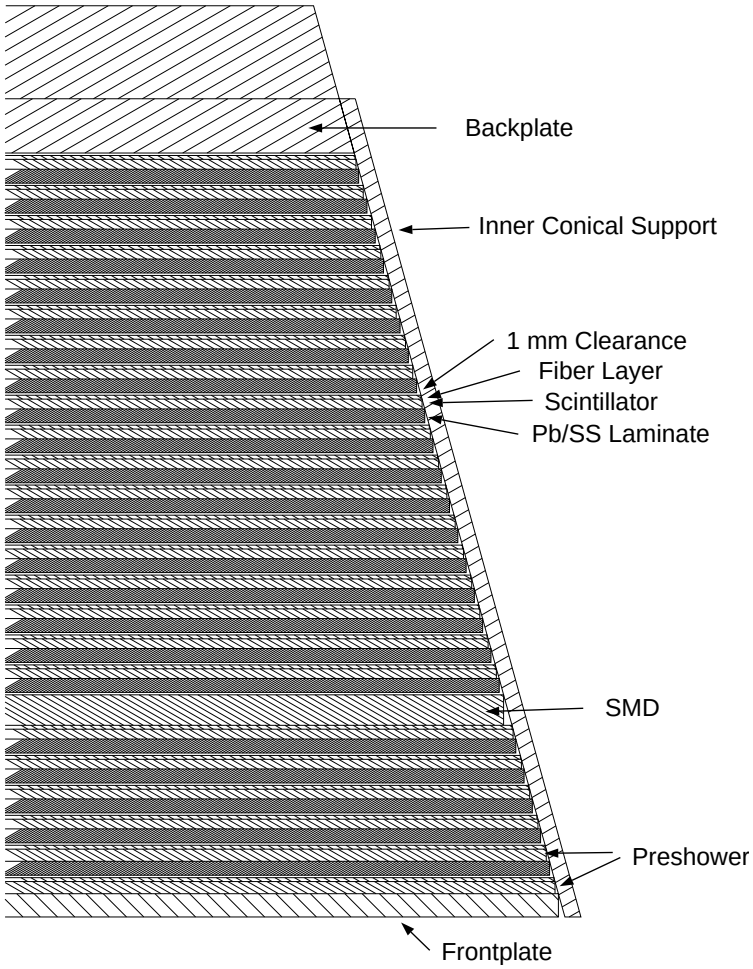

Figure 10: *A cut through the EEMC near η=2. The mechanical structure as well as the absorber scintillator layers are shown.*

2.3 Active Elements of the EEMC

The advantages of building the EEMC as a Pb/scintillator sampling calorimeter are cost, simplicity and sharing of technology with the BEMC. A cross section of the layers of the detector is shown in more detail in Fig. 10. There are 23 layers of Pb/SS laminate that serve as the primary radiators and an aluminum front and stainless steel back plate for mechanical structure. The sampling at each layer is done with a scintillator whose light is collected and transported by a wave length shifting (WLS) fiber. A standard layer in this design comprises Pb/stainless steel

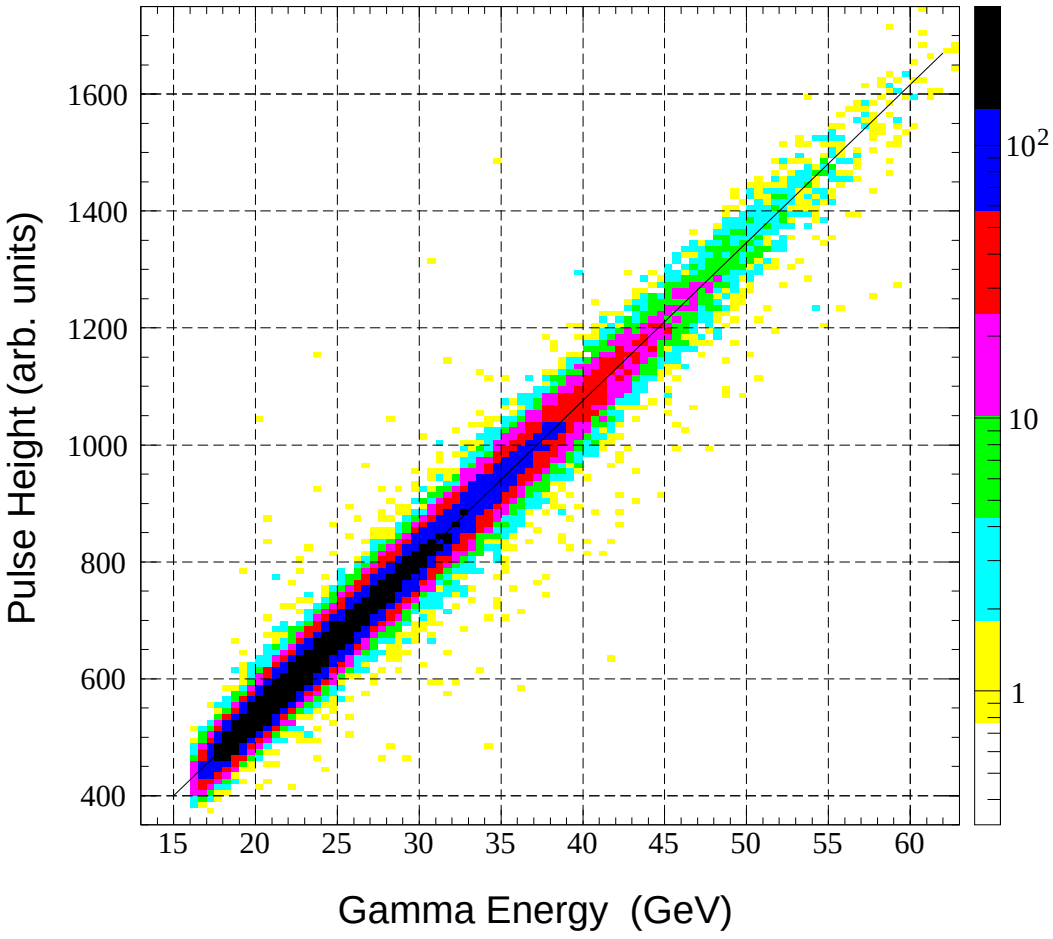

Figure 11: *Linearity of the endcap calorimeter response to photons over the energy range of interest for direct photon production at 200 GeV. The simulation includes photons incident on all towers of the endcap. It assumes perfect gain-matching among scintillator tiles within a given tower and accurate tower-dependent energy calibrations.*

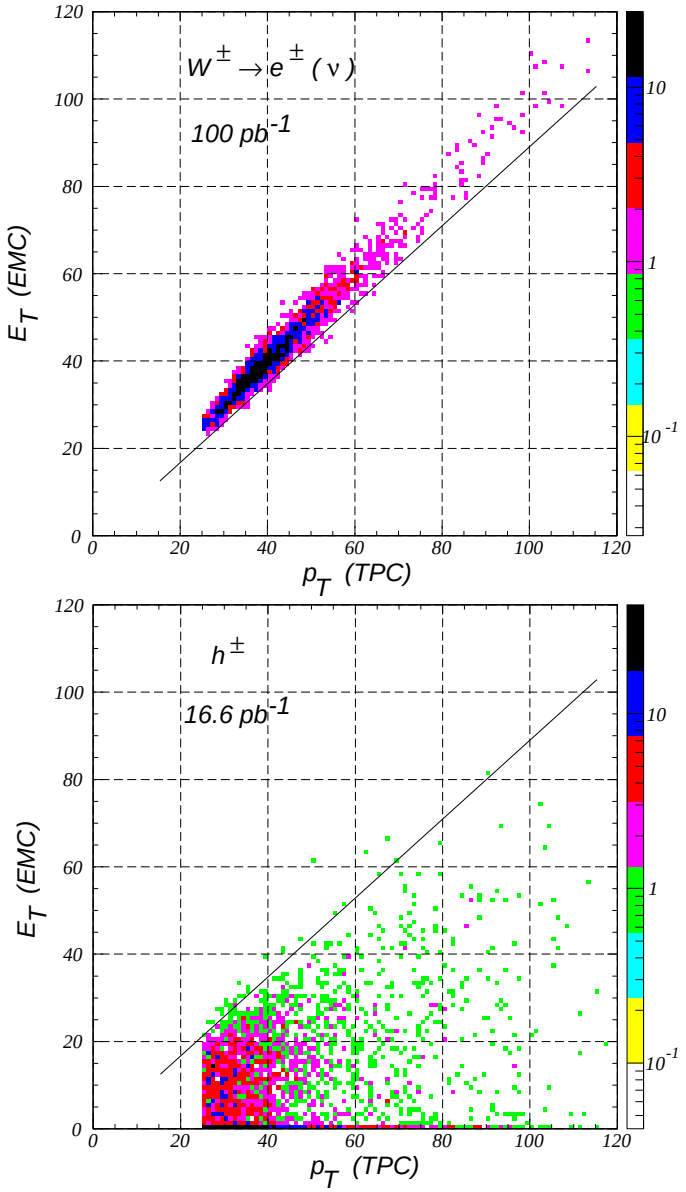

Figure 12: *The simulated correlations of energy measured in the EMC with momentum determined from the TPC for W decay daughters and for hadrons. The straight line represents a cut used for electron/hadron separation. The simulations included only events with* $p_T > 25$ *GeV/c.*

(SS) laminate (4.68 mm Pb, cladded by two 0.5 mm stainless steel sheets, for a total of ~0.85 radiation lengths) followed by a 4mm scintillator, a 1.6 mm plastic sheet for fiber routing and 1 mm of clearance. The whole assembly represents 21 radiation lengths at normal incidence. Since the particles actually traverse the detector at an angle, they see 21.8 radiation lengths at η=2 and 27.6 radiation lengths at η=1. In addition the TPC end plates represent about 1 radiation length of material (on average) that must be traversed before particles reach the EEMC. This sampling fraction and total depth are driven by a combination of physics requirements and a predetermined space budget at STAR; in fact they also closely match those values used in the CDF endcap electromagnetic calorimeter [33]. Figure 11 shows a simulation of tower pulse height vs. the energy of direct photons expected for pp$\rightarrow \gamma$+ Jet + X events at $\sqrt{s}$=200 GeV. This performance is clearly adequate for the ΔG measurements. Fig. 12 shows simulations for $W^{\pm}$ production at $\sqrt{s}$=500 GeV, resulting in the highest energy electrons and positrons that will be detected by the EEMC. Even for these high energy particles, the response of a 21 radiation length detector is mostly linear.

As summarized earlier, the calorimeter is segmented into 720 projective towers by dividing each scintillator layer into tiles which align properly with the corresponding tiles in front and behind to form the towers. The tile segmentation produces projective towers spanning 0.1 in azimuthal angle (ϕ) and either 0.05 or 0.1 in pseudorapidity (η), as shown in Fig. 8. Due to a gap in the detector at η=1, needed to bring utilities and support structures to the central detectors, the EEMC covers the approximate range $1.07 \leq \eta \leq 2$.

Three of the EEMC layers are configured in a special way:

1) The first two layers of scintillator immediately after the front support plate are each read out by two independent fibers. One fiber in each case is routed to the phototube that measures the total light produced by the tower. The second fiber from each of these layers is read out separately, to form a preshower detector, to aid in γ/π^0 and e/hadron discrimination. The scintillators in the first two layers are increased slightly in thickness (5mm) to account for the lower light output in each fiber when two are used on the same tile. The same 1.6 mm plastic layer and 1 mm clearance are provided in these layers.

2) The third special layer will be placed about 5 radiation lengths deep in the detector. This layer includes a shower max detector (SMD) in addition to a standard 4mm scintillator layer. In the present design, the SMD location is similar to that found in other working EM calorimeters. Further simulations are ongoing, however, in order to optimize the SMD location, particularly with regard to the question of optimizing the γ/π^0 discrimination at the highest energies in the endcap. (Note: The actual SMD placement does not change critical endcap design parameters or integration issues, e.g., overall depth budget, fiber routing, etc., so altering its placement has no real impact on the overall conceptual design).

The shower max detector is to be made of extruded triangular scintillator strips (1 cm base, 0.5 cm height) organized into orthogonal U and V planes as shown in Fig. 9. The triangular cross section induces a sharing of the energy deposition among adjacent strips which enhances the position resolution and is important for γ/π^0 discrimination (Sec.A.3.2). Such a design and similar techniques have been developed by D0 for use as a tracking preshower detector [34]. The SMD scintillators are segmented into 30° sectors. The WLS fibers for the SMD run axially along the length of each strip, through holes created during the extrusion. After exiting the end of the scintillating strips, the fibers curve across the neighboring 30° sector. Pairs of adjacent 30° sectors will form self-contained 60° units for assembly. Adjacent 30° sectors are staggered in depth by 2.5 mm to allow the fibers from one sector to be routed on the top or bottom surface of

the neighboring layer, as they curve their way toward the outer circumference. Our simulations show that cuts based on this SMD detector can reject up to 80% of 30 GeV $\pi^{\circ}(\eta)$ events, at the expense of cutting out only about 20% of single photons (see Sec. 3.3). Neither a gas SMD, such as planned for the BEMC, nor one based on rectangular scintillating strips, can match this simulated performance for the high-energy photons of interest in the EEMC region.

As described above, the scintillator at each layer is segmented into tiles. Towers projective toward the interaction point are made up by summing the light from the 24 tiles (one from each scintillator layer) stacked up one behind the other. At each layer, 12 tiles of different size provide the η segmentation. In addition, in order to define fixed η ranges, the tiles within each tower grow in size with increasing depth. The segmentation will be produced using megatile construction as developed and used for CDF [35] and adopted for the BEMC in STAR [36]. In this technique a large piece of scintillator, a 6° wedge in ϕ for the EEMC, is machined with a router most of the way through its depth in order to separate one tile from the next. The grooves are filled with TiO_2 loaded epoxy to give good optical isolation from the adjoining tiles, as well as to restore the mechanical strength. The edge of the megatile is painted with TiO_2 reflective paint and the large surfaces covered with paper to complete a diffuse reflective surface for each tile. Wavelength-shifting optical fibers are inserted into "σ"-shaped grooves machined in the face of each tile, and then run radially to the outer edge of the plane through thin plastic guides on top of the plane. At the edge, the WLS fibers are attached to clear fibers with commercially available connectors. Each of the 24 scintillator planes comprises 60 such megatiles.

2.4 Mechanical and Structural Issues

The EEMC must include a strong structure that allows the detector to be assembled horizontally and then lifted and rotated to hang vertically on the pole tip of the STAR magnet. On the other hand, structural members must not generate large dead regions in the detector. One way of addressing this problem is to provide a strong back plate and a central hub on which most of the detector weight hangs. Our intention is to take over such a design strategy, used by both D0 [37] and CDF [33]. A 7/8" thick stainless steel backplate is employed with a 1/4" wall conical (to match η=2) tube welded to it. (Note: non-magnetic types of stainless steel are necessary throughout in order not to perturb the magnetic field of the solenoid.) Of particular concern are deflections at the inner radius where the tube joins to the backplate. Too large a deflection here could press on the correction coils which are sandwiched in the pole tip behind the EEMC backplate. However, there is about 1.5" free behind the backplate which will allow for its reinforcement in this area and clearance from the coils. The above dimensions are chosen based on an early design concept by ANL [38] which included some finite element (FEA) calculations. Complete engineering and design, including FEA, will be carried out on such issues as we move past this conceptual stage.

The second structural issue is that Pb is a difficult material to work with. It is not particularly strong and tends to creep over time if stressed. To solve these issues we intend to follow a technique used at CDF [33], laminating the Pb with stainless steel. That is, a half annulus of 4.7-mm thick Pb is clad by epoxying 0.5 mm stainless steel to the surface, on each face. In addition, stainless steel inserts will be placed in the lead and spot welded to the SS foils at points around the circumference and on radial lines every 30°, in order to provide solid points to transfer the load to the other structural members. Bolts will pass through a 3/8 inch aluminum front plate of the EEMC, and the 23 layers of lead/steel sheets and intervening stainless spacers,

to support the lead radiators and maintain the separation between them needed for insertion (without compression) of the scintillator tiles. A stainless steel ring is welded in place at the inner circumference to sit on (and gain support from) the inner support hub which is welded to the back plate. In its entirety, this provides a structure in which all the large loads are carried primarily by stainless steel and the Pb just serves as the filler in the laminated plates. Such a design should be quite robust. From discussions with CDF design engineers (Jim Kirby of FNAL), we learned that they estimated sag at several tenths of a mm in the horizontal orientation, and furthermore, they were able, without significant difficulty, to assemble their endcap by sliding in the megatiles and fibers, as we plan to do.

It should be mentioned that an alternative option is also being explored. That is to use tungsten as the radiator and basis for the support structure. It certainly would be much stronger than the Pb/SS laminate, but more importantly, it would clearly alleviate the depth budget contraint, vis-a-vis detector radiation length, if the material could be obtained and machined at a cost competitive to the present design. At present, this option is viewed as extremely beneficial, though not mandatory for a fully adequate EEMC constructed within the allowed integration volume.

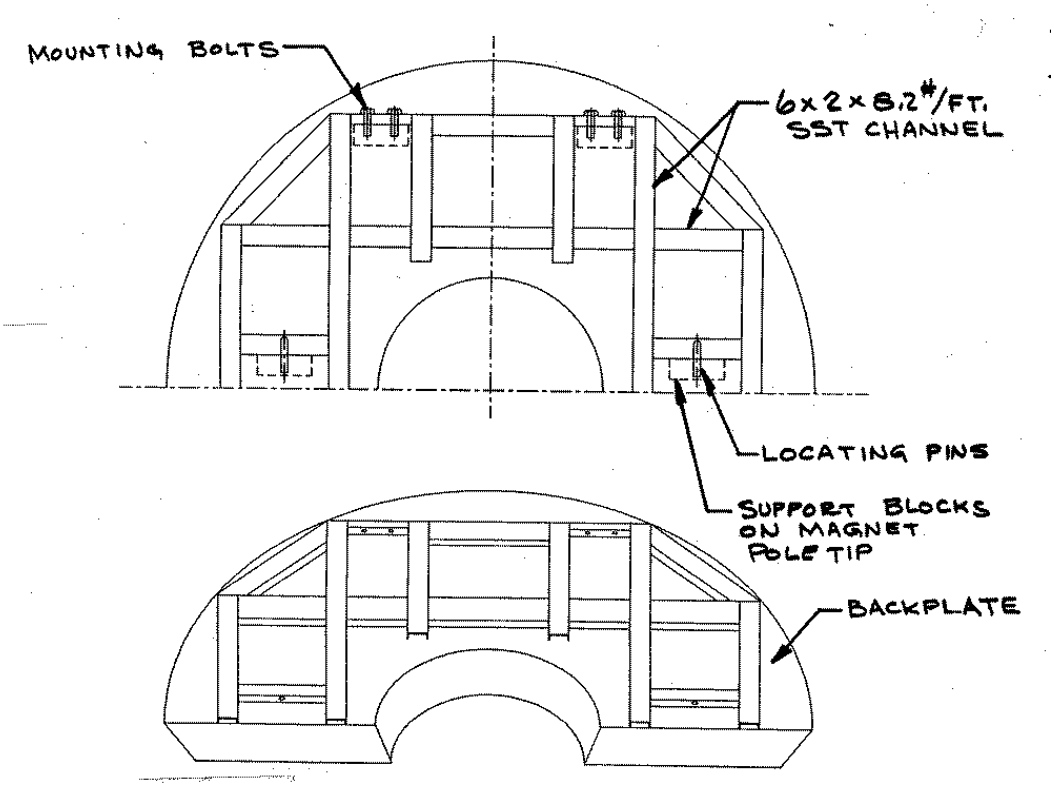

Figure 13: *Conceptual design for mounting the EEMC to the magnet poletip taken from STAR Note 120 [38]. The mounting bolts will be relocated as appropriate to the vertical orientation proposed here for each half of the endcap.*

Mounting to the poletip will be done with pins and bolts, as shown in Fig. 13, a concept from

an early design at ANL [38]. 1.5 inch clearance is left behind the back plate of the calorimeter to attach stainless steel channel and bar stock for support surfaces and reinforcement. Existing tapped holes on the poletip will be used to attach mating surfaces for the support structure on the back of the calorimeter.

The full EEMC will have an outer diameter of about 5 meters and weigh over 20 tons. We intend to segment the detector into two halves along the vertical centerline. This may complicate the structural design issues slightly but will make assembly and handling considerably more convenient. It will also allow for a staged approach in construction. We note that there is a 30° segmentation in both the TPC and endcap SMD. Splitting the detector along the vertical line forces the shadow of the TPC supports to fall in the center of the SMD sectors. Therefore, we will consider segmenting the endcap along a line 15° from vertical, to have these shadows fall along the borders between SMD sectors if simulations (or indeed, other considerations) show a significant advantage to doing so.

2.5 Optical Systems

A total of nearly 26,000 clear optical fibers will be run in flat ribbons to the rear of the poletip, through gaps at the outer circumference foreseen for this purpose. Light-tight cooled boxes for the photomultiplier tubes (PMT) will be permanently mounted on the outside surface of the poletip as shown in Fig. 14. The 24 fibers from each tower are routed to a single-anode PMT, which gives a signal proportional to the total energy deposited by the shower within that tower. Fibers from the preshower and SMD scintillators will be routed to 16-anode PMT's. Some detailed considerations for the general design follow.

A standard layer of the end cap calorimeter uses 4mm thick Bicron BC408 scintillator. The depth restriction limits the thickness of these tiles and thus Bicron scintillator is chosen for its higher light output over the Russian scintillator used in the barrel [36]. CDF uses Kuraray SCSN38 polystyrene scintillator of 4mm thickness [33], which has a light output midway between the Russian and Bicron scintillators [39]. Sigma-shaped grooves are machined into each tile to capture 0.83 mm diameter wave length shifting fiber. A 1.6 mm layer of plastic with machined (or "press in") grooves is placed on top of each megatile to serve as a fiber routing layer. At the outer edge of a megatile, the 12 fibers are attached to a multifiber optical connector similar to those developed for CDF [40]. For the preshower (the first two megatiles), each tile has two fibers in the groove and so 24 WLS fibers run to the outer edge of each of these megatiles. We are still searching for a proper optical connector that will carry 12 fibers economically. We envision that the megatile and fiber routing layer with connectors will be made as one assembly. These assemblies will then slide between the Pb/SS layers after the mechanical construction.

The shower max layer presents special problems for fiber routing. There are many fibers in one plane and they exit midway in depth through the plane. As described in the above section, we will build the SMD in 30° sectors with adjacent sectors alternating in depth by half their thickness. The fibers will then leave their respective strips along the radial border between neighboring sectors, and be routed to the outer circumference along the surface of the neighboring sector. Since the SMD sectors become interconnected in this way, the SMD must be assembled into the mechanical structure and will not be as easily removable as the megatiles. In addition, the outer edge of the SMD layer will be densely populated with optical fiber connectors in order to couple out the $\geq$600 fibers per sector.

The detectors will be read out by photomultiplier tubes mounted in boxes on the outer

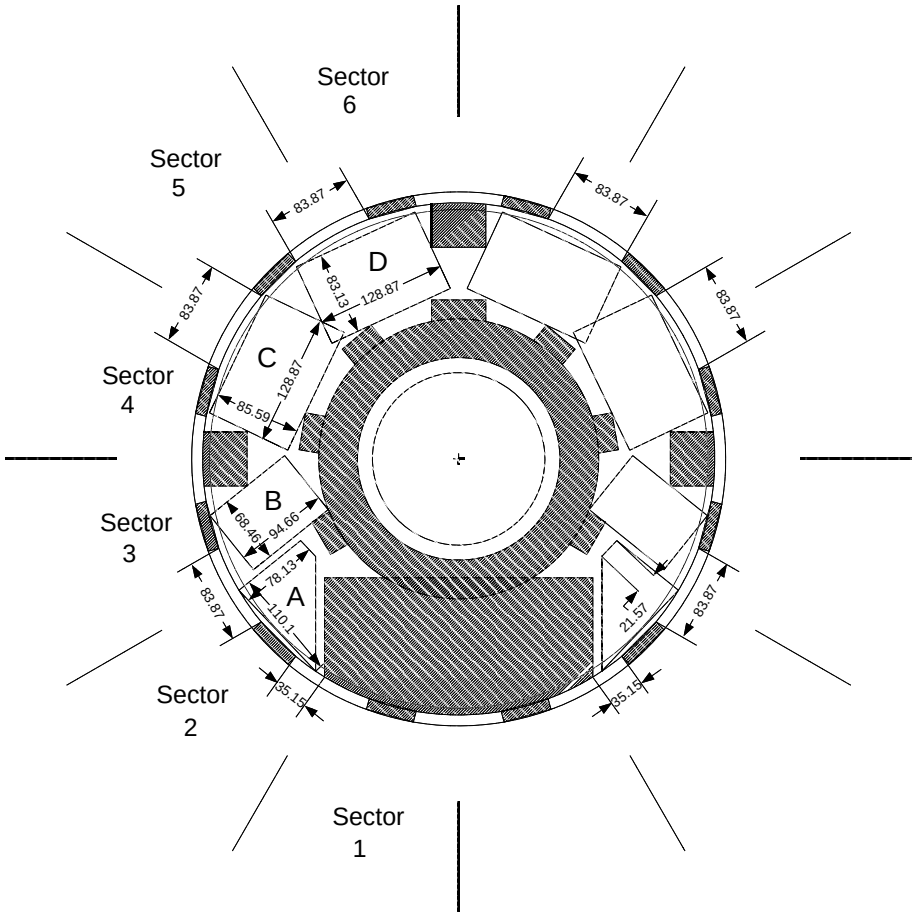

Figure 14: *View of the outside poletip surface. Areas ruled out by integration are shaded. The outermost annulus is the services gap. The lengths of unoccupied regions of the gap are indicated. Regions where cable trays have been installed are also shaded. Six 30° sectors of the SMD are labeled on the left side of the poletip. The boxes A-D are shown to estimate the area available for mounting PMT boxes on the poletip surface.*

face of the magnet poletip. The light will be transported from the detector to these PM boxes via clear 0.93 mm diameter fibers joined into ribbon cable bundles with a plastic coating and terminated with commercial connectors at both ends. These fibers will be routed after the detector is mounted on the poletip. Fiber ribbons leaving the edge connector of a megatile will turn to travel on the circumference of the EEMC to the point where they will exit through the services gap at $\eta \sim 1$. They then run on to the outside surface of the poletip where they enter the proper PMT box. Details on the amount of space needed for the fibers are provided in a subsequent section.

Tower fibers are naturally routed from the detector grouped by megatile. They need to go to the PMT's grouped by tower. We will use a mixing box to reroute the fibers before they are patched to the PMT boxes. The 24 fiber ribbons containing the fibers from all tower tiles (neglecting the preshower, which will be handled separately) within a given 6-degree sector will

be collected, one above the other, into two groups of 12 ribbons. Each group can then be viewed as a 12 x 12 matrix of fibers, each row (incoming ribbon) corresponding to one megatile and each column to one tower. The rebundling/regrouping simply consists of separating the fibers from their incoming horizontal ribbons and rejoining them into vertical ribbons which culminate in a 12-fiber tower connector. Two of the outgoing tower ribbons will run to each PMT for the towers. In addition, to simplify the routing in the PMT boxes, the mixing box will make it possible to easily connect diagnostics to individual towers.

The longest WLS fiber run to the edge of a megatile is about 1.6 m for the large-η tiles. Clear fiber can be thermally fused to the WLS fiber to prevent too great an attenuation of light for long WLS fiber runs. This will be pursued as necessary. This technique also allows for the correction of ℓ/A scaling of light output from the tiles at different depths in the tower by adjusting the length of WLS vs. clear fiber. The longest run of fiber from megatile edge to the PMT boxes is for the megatile at 6 o'clock. This is estimated to be 2.5 m, with up to an additional 1 m inside the PMT box. These fiber runs are very similar to those quoted for the CDF endcap upgrade, where they achieve sensitivity exceeding their design goal of 3 photoelectrons/minimum ionizing particle [35]. Similar performance for the EEMC would exceed our requirements.

2.6 Electronics Issues

Much of the readout and trigger electronics under development for the barrel EMC (described in Ref. [36]) can be taken over without significant modification for the endcap. Allowance for triggers of interest for the spin program, as discussed in Sec. 3 below, is already included in the plans for the barrel front-end electronics, and will be implemented for the endcap as well. Pulse height information from the EEMC towers will be digitized in 12-bit flash ADC's for every beam crossing, and the results will enter into (dead-timeless) pipelines for subsequent processing. The STAR hardware (level 0) trigger has allowance to compare a subset of this digitized energy information to various thresholds. Although the exact nature of these choices is still evolving for the BEMC, the information to be used for level 0 will include the sum (most significant six bits) of energies deposited in non-overlapping calorimeter "patches" of size $(\Delta\eta, \Delta\phi) \leq (0.2,0.2)$, and the largest energy (again in six bits) deposited in a *single* tower within each such patch. For events that pass the trigger, recording of the full 12 bits of ADC information for individual towers will provide more than adequate energy resolution and will allow us (barely) to span the full 1000:1 dynamic range from single minimum-ionizing particles (MIP's, useful for system calibration) through $W^{\pm}$ decay daughters with up to 150 GeV ($p_T \approx 40$ GeV at $\eta \approx 2$, leading to ≈ 10 GeV energy deposition in the tower scintillators). In comparison with the EMC towers, both the preshower and shower-maximum detectors will exhibit much smaller dynamic ranges in output pulse height, so that fewer bits per channel, but many more channels (≈ 8600 for preshower and SMD combined) will be needed. It is not envisioned that the preshower and SMD information will be available for the level 0 trigger. The digitization electronics in this case will be modeled after that developed for other STAR subsystems (the SVT and TPC).

2.7 Integration Issues

The EEMC must fit within the predefined integration volume indicated in Fig. 7. The allowed depth, 37.45 cm, begins at the inner surface of the poletip. A 1.3 cm clearance volume must be maintained in front of the EEMC to allow for a "rocking" motion during insertion of

the pole tip. The depth limitation is the primary constraint on the thickness of the calorimeter. The current design is 1 mm below this limit. The $\sim$ 1 mm clearance currently left between each layer of the calorimeter should allow sufficient design flexibility for us to maintain the total current 21 radiation length as the mechanical design proceeds. (We note again, that use of tungsten radiators would effectively erase any depth budget concerns).

The outer diameter of the EEMC is limited by an integration line parallel to η=1 but translated by 5 in. toward smaller angles. Our present design of the EEMC leaves the outer 2 cm near this line for fiber routing, so that the the EEMC active region begins at η=1.07. This decision will be revisited as 3-D models of the fiber routing are developed. The integration volume is also limited at η=2 and our current design reflects this. An additional 1 in. beyond η=2 is assigned to the EEMC for routing cables and fibers. Since the inner radius of the EEMC is used in our design as a primary structural support, we do not envision bringing fibers out on this surface. We thus use this fiber routing space for the mechanical structure and can then have active detector out to η=2.

There are many other issues related to the integration of the EEMC with the STAR detector, beyond the question of fiber routing. These issues have been addressed in some detail in the recent STAR internal review of this proposal. Some of the considerations include:

- The size and number of the light-tight boxes used to house the tower readout, SMD and preshower PMT's. These boxes will be attached on the outside of the west-end poletip of the STAR magnet. At issue is the space available for these boxes, so that they can remain in place during roll out of the STAR detector from the RHIC ring. Adequate space is available. In a related issue, for all poletip moving scenarios, the fibers remain connected to the calorimeter mounted on the inner face of the poletip, and the PMT's mounted in the boxes on the back face.

- The magnitude of the magnetic field in the region of the PMT boxes near the $\eta = 1$ gap is difficult to calculate reliably and may be significant. The field on the outside of the poletip will be measured when the field mapping of the STAR magnet begins. Care must be taken that exterior shielding measures don't affect the interior fields.

- In addition to the PMT boxes to be mounted on the exterior of the poletip, $\sim$ 10 VME crates worth of front-end electronics must also be mounted there so as to be in close proximity to the PMT's. A scheme for this mounting, allowing minimal disruption of cabling and services during poletip removals for most STAR detector servicing, was presented.

- The total volume available at the $\eta = 1$ service gap near the edge of the west poletip of the STAR magnet is an issue. As part of the STAR review, a detailing of how the EEMC fibers will be routed through this gap, along the edge and around to the back of the poletip was provided. Only a small fraction of the available volume in the $\eta = 1$ service gap is required for the fiber bundles associated with the EEMC.

- Electronics integrations issues ... no significant differences are foreseen between the needs for the EEMC and those of the BEMC; for the latter, many of the engineering designs for the required electronics are underway.

3 Performance Issues and Simulations

The physics goals of the $\vec{p}-\vec{p}$ and $p-A$ experiments to be carried out with STAR, enhanced by the barrel and endcap calorimeters, establish a number of critical performance demands on the detector. It must be demonstrated that suitable statistical precision can be attained at luminosities the detector and readout can handle. This requires trigger logic based on the fast detector components that is capable of selecting the most interesting 0.001% of all $\vec{p}-\vec{p}$ collisions to initiate readout of the slow TPC. Even at suitably reduced trigger rates, the TPC will register track segments from events occurring within ± 40 μs of the trigger, representing products from hundreds of undesired beam crossings; these extraneous tracks must be subject to rapid software rejection. Efficient identification of jets and determination of their central rapidity and, to a lesser extent, of their total momentum are important elements in much of the physics program. It is vital to the measurement of the gluon spin distribution that directly produced photons be distinguished adequately from photon pairs arising from neutral meson decay. A clean distinction between electrons or positrons and charged hadrons is central to the $W^{\pm}$ production, while separation of W^+ from W^- events must rely on adequate TPC resolution to distinguish the sign of the curvature of quite rigid tracks. Reliable experimental determination of the Bjorken x-values for the colliding partons depends on accurate absolute calibration of the energy scale for the calorimeter towers. The entire spin physics program requires a clear understanding and monitoring of instrumental asymmetries and absolute calibration of beam polarizations in an energy regime where these topics are essentially unexplored. In this section we explore each of these demands in turn, and outline the approaches that we believe will guarantee success, and the simulations which support this conclusion. Simulation results for photon-jet coincidence studies are described in much more detail in the Appendix.

3.1 Rate Capabilities

The simulations presented in this proposal are based on integrated $\vec{\mathrm{p}}+\vec{\mathrm{p}}$ luminosities that have been established as standard values for the RHIC spin program: 320 pb^{-1} at $\sqrt{s}$=200 GeV and 800 pb^{-1} at 500 GeV. These integrated luminosities correspond to 10 weeks of running time at each energy, with roughly one third of the time lost to overhead and problems, at the ultimate luminosities expected for the polarized proton collisions: 8×10^{31} cm^{-2}s^{-1} at 200 GeV and 2×10^{32} cm^{-2}s^{-1} at 500 GeV. At these full luminosities, minimum-bias pp collisions will occur at total rates of $\approx$ 4 MHz and 12 MHz, respectively. In contrast, the TPC information cannot be read out at rates exceeding about 60 Hz. Thus, a fast hardware trigger must effect a large reduction in the rate of collisions processed.

The barrel and endcap EMC's will play the essential role in defining hardware triggers suitable for the spin program. The hard photons and electrons of interest can be identified relatively cleanly by their characteristic large energy deposition in a narrow patch of the calorimeters. For example, simulations [41] demonstrate that the trigger rate is reduced by four (of the required five) orders of magnitude by requiring that there be a transverse energy deposition of at least 10 GeV in one or more $(\Delta\eta,\Delta\phi)=(0.2,0.2)$ patches. A suitable high-efficiency trigger for the direct photon and $W^{\pm}$ production events of interest could be attained by adding the requirement that the highest single-tower energy deposition within that patch carry a large fraction of the 10 GeV. If necessary, the trigger rate could be reduced further in Level 1 processing by adding an "isolation" cut, *i.e.*, by placing an upper limit on the energy deposition in surrounding patches.

The above trigger would discriminate against most of the abundant dijet events, because jet energies are typically spread over a much broader patch of the calorimeter, and are concentrated in hadrons to which the calorimeter response is much weaker. Thus, a separate jet or dijet trigger will be needed. The most promising jet trigger appears to be one exploiting the correlation between two characteristics of the typical jet: localized enhancements in electromagnetic energy (as measured in the EMC's) and in charged-particle multiplicity (as measured in the Central Trigger Barrel for $|\eta| \leq 1$ and in the Multi-Wire Chamber at the end of the TPC for the endcap region). Correlated conditions can be imposed on these measured quantities on a patch-by-patch or sector-by-sector basis in STAR's Level 1 trigger. Preliminary simulations suggest that such correlated conditions can readily reduce the minimum-bias event rate by three orders of magnitude, while retaining trigger efficiencies well in excess of 50% for dijet events generated (with the code PYTHIA [42]) from partonic collisions at $p_T \geq 10$ GeV/c. Further background trigger rate reductions could be effected (also at Level 1) by requiring jet-like clusters in two detector patches at roughly opposite ϕ-values. The resulting rates would be acceptable for early dijet runs at reduced $\vec{\mathrm{p}}\vec{\mathrm{p}}$ luminosities. However, at the enhanced luminosities needed for the photon and W production programs, dijet trigger rates will have to be reduced further, for example, by prescaling those triggers corresponding to the relatively abundant dijets near the lower end of the accepted p_T range.

Even when the trigger rate has been reduced to the desired level, the slow drift time ensures that the TPC will record track segments arising not only from the beam crossing which generated the trigger, but also from uncorrelated events that occur within $\approx \pm 400$ bunch crossings. At full luminosity, this pileup will lead to somewhere between 1000 and 4000 undesired tracks. The resultant TPC occupancy will then be comparable (though less dense near the center) to that for a single central Au + Au collision, which, fortunately, the TPC was designed to resolve. As detailed in Ref. [43], the vast majority of undesired tracks can be eliminated rapidly because they fail by large margins to line up with the EMC and Central Trigger Barrel hits recorded during the trigger beam crossing, or with physically reasonable vertex locations. Finer matching can be done in subsequent analysis by combining TPC with SVT information to achieve vertex resolution better than 1 mm (roughly 1% of the interaction diamond length) and by using the SMD for electrons to provide good spatial resolution (≈ 2.5 mm for the endcap) on the EMC hits. With these resolutions one can even discriminate effectively against tracks from multiple events *within the same crossing*. The analysis in [43] suggested that pileup tracks that cannot easily be distinguished from the desired tracks should yield less than a 1% contamination. We are planning more sophisticated simulations, incorporating all presently envisioned STAR components and presently implemented reconstruction algorithms, to reevaluate the TPC pileup elimination.

The pileup does require that serious pruning be performed on the TPC information before writing an event to tape, in order that the maximum foreseen data acquisition bandwidth not be exceeded. The pruning will be done in the Level 3 trigger [44] already under development for STAR. The imposition in Level 3 of higher-level correlated conditions on the information from various detector components is expected to reduce the event rate for pp running from ≈ 60 Hz at the input to 10–20 Hz at the output. Still, an additional reduction by an order of magnitude in event *size* will be needed to reach acceptable data rates (below 20 Mb/s). This will require the elimination of most pileup tracks (*e.g.*, those that clearly do not point toward the interaction diamond) in Level 3 software. In addition, it may require that only the TPC clusters identified at Level 3, and not the raw TPC hit information, be stored for the surviving tracks. The latter option might lead to a slight deterioration in TPC resolution achievable for pp running. The

enhanced pp luminosities that will necessitate the event size reduction will become available only in year 3 or 4 of RHIC operation; optimal Level 3 algorithms will be developed in the intervening period.

3.2 Jet Identification and x_{parton} Reconstruction

Jets are identified operationally as clusters of particles depositing large cumulative transverse energy E_T in a confined solid angle. For the purpose of simulations reported here, we have considered jet cones of half-angle $\sqrt{(\Delta\eta)^2 + (\Delta\phi)^2} = 0.7$, and required a minimum jet energy of 5 GeV [45]. Fluctuations in jet characteristics make their absolute cross sections sensitive to these parameters, but as long as the fluctuations are spin-independent, polarization observables should not exhibit similar sensitivity to details of jet identification. It is the substantial cone angle that makes the large acceptance of the STAR detector so essential for jet reconstruction.

While STAR does not have a hadron calorimeter, the momentum of charged hadrons within the jet can be determined with comparable resolution from the TPC tracks, whereas that of neutral hadrons that decay electromagnetically will be determined from the barrel and endcap EMC's. Corrections will have to be applied for the unmeasured momentum of other neutral hadron (n, $\overline{\rm n}$, $\rm K_L$) components. Appreciable uncertainties in jet momentum determination arise from fluctuations in the fraction of momentum carried by such undetected particles (including also those falling within gaps in the EMC coverage) and, especially in the endcap region, from the TPC resolution. However, these STAR-specific resolution contributions remain significantly smaller than a fundamental limit imposed by the physics of parton fragmentation: even with perfect detector resolution, events generated with PYTHIA exhibit a 30% (FWHM) spread in the correlation of jet energy with that of a single final-state parton in the hard collision.

It is important to emphasize, however, that the jet momentum is not necessary to reconstruct the Bjorken x-values of the colliding partons for each γ-jet coincidence event. For this purpose, it is sufficient to use the central jet *direction* (i.e., pseudorapidity $\eta_{\rm jet}$), which is determined with much better resolution than the momentum, and has a more direct connection to the behavior of a single parton. In particular, if we assume two-parton kinematics, neglecting any *transverse* momentum of the colliding partons in the initial state, then we have:

$$x_{1(2)} = \frac{p_T(\gamma)}{\sqrt{s_{pp}}}[\exp(\pm\eta_\gamma) + \exp(\pm\eta_{\rm jet})]; \tag{2}$$

$$|\cot\theta^*| = |\sinh(\frac{\eta_{\rm jet} - \eta_\gamma}{2})|, \tag{3}$$

where we use the (EMC) momentum measurement for the photon only, and θ^* is the photon angle with respect to the incident quark in the partonic c.m. frame. The resolution of the above reconstruction is typically $\delta x_{1(2)} \simeq 0.02$ (FWHM). The corresponding resolution is quite a bit worse for dijet events, since there we must rely on p_T measurements for the jets.

Kinematics alone cannot resolve the ambiguity regarding *which* of the colliding partons to associate with x_1 and which with x_2, nor the resulting ambiguity in the sign of $\cot\theta^*$. In the case of the dominant Compton scattering process for photon production, we make a simplifying assumption in the analyses of simulations presented here, namely, $x_g = \min[x_1, x_2]$. This assumption is generally supported by both the unpolarized parton distribution functions within a proton and the differential cross section for gluon Compton scattering. In Sec. 3.6.1 below, we discuss systematic errors arising from this and other simplifying assumptions in the analysis.

3.3 Identification of Direct Photons

A crucial issue in determining the polarized gluon structure function is the experimental distinction between directly produced photons and closely spaced photon pairs resulting from the electromagnetic decays of neutral mesons, especially π^0 and η. At the energies of interest, the most probable lab-frame opening angle between the two photons, $\phi_{\gamma\gamma}^{min} = 2\sin^{-1}(m/E)$, can be as small as 10 mrad. Furthermore, the mesons are produced with significantly larger cross sections than the direct γ's, as part of the fragmentation of hard-scattered quarks and gluons. Fortunately, the known quark and gluon fragmentation functions indicate only a small probability for a single π^0 or η to carry the majority of the momentum of the final-state parton, and even then, high-p_T mesons are generally accompanied by other charged particles or photons to form a jet. Hence, the first level of distinction between direct photons and $\pi^0(\eta)$ mesons is to apply an isolation cut, requiring minimal energy in accompanying charged particles or photons in a cone around the direct photon candidate. (The isolation cut also greatly reduces the contributions of fragmentation photons to the direct photon sample [9].) The efficacy of the isolation cuts is aided by the large acceptance of the STAR detector, but, as shown below, they are not sufficient to identify direct photons cleanly. It is therefore essential that the EEMC have a state-of-the-art shower-maximum detector to further distinguish single photons from photon pairs.

The ratio of total production cross sections for high-p_T $\pi^0(\eta)$ mesons vs. direct photons can only be estimated from data acquired with other collider detectors. Such estimates [46] suggest $\sigma_\pi : \sigma_\gamma \sim 5 : 1$ over the ranges $-1 < \eta < 2$ and $10 < p_T < 20$ GeV/c for $\sqrt{s} = 200$ GeV pp collisions, with little information on the dependence of this ratio on pseudorapidity or isolation cuts. To address these questions, we have simulated the production of π^0 and η mesons with the code PYTHIA [42], by examining all fragmentation products resulting from $2 \to 2$ partonic hard-scattering processes allowed in a pp collision. We compare this yield with that computed for direct photons, arising from $qg \to \gamma q$ (predominantly) and $q\overline{q} \to g\gamma$ or $\gamma\gamma$. The simulation result for the expected background:signal ratio is in qualitative agreement with the data extrapolation: $\sigma_\pi : \sigma_\gamma \approx 8 : 1$ and $\sigma_\eta : \sigma_\gamma \approx 4 : 1$. The variation of these ratios with pseudorapidity is small (Fig. 15). Figure 15 also illustrates the effect of an isolation cut, which reduces the net ratio from 12:1 to about 3:1, by removing 78% of the mesons *vs.* 14% of the photons. The isolation cone used (half-angle $\sqrt{(\Delta\eta)^2 + (\Delta\phi)^2} = 0.26$) was based on the UA2 analysis [47] of direct photon + jet coincidence yields in unpolarized $p\overline{p}$ collisions at $\sqrt{s}$=630 GeV. Events were rejected if they were accompanied by *any* additional charged particles or photons within this cone, independent of their energy deposition. We have not yet explored optimization of the isolation cut.

The shower-maximum detector (SMD) allows additional event-by-event discrimination between single photons and photon pairs on the basis of the measured transverse profile of the electromagnetic shower. Its response has been simulated with the code GEANT [48], assuming that the SMD is positioned after 5 radiation lengths of material within the EEMC, and that each scintillating strip generates an average of two photoelectrons per minimum-ionizing particle traversing its (maximum) depth. Typical responses for a single photon and a π^0 are illustrated in Fig. 16.

SMD discrimination against mesons is incomplete because of shower-to-shower fluctuations and very asymmetric meson decays, where one of the daughter photons has quite low energy. Optimal discrimination requires a sophisticated analysis algorithm. Here, we have made cuts

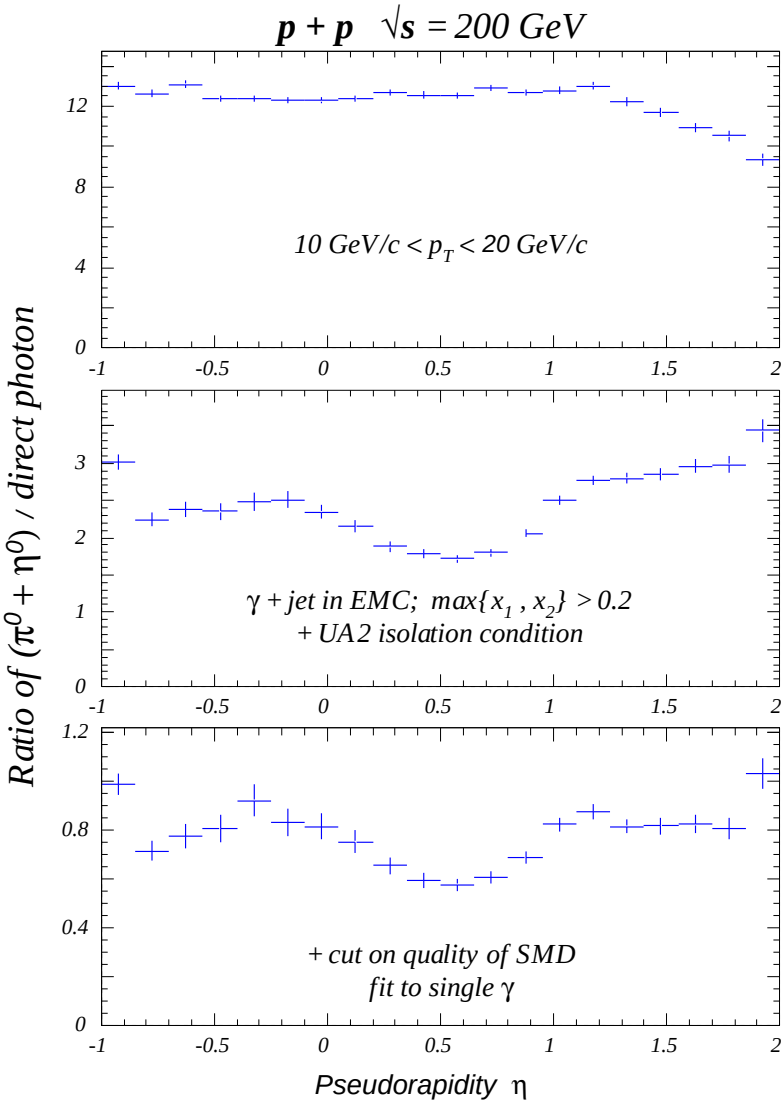

Figure 15: *Cross section ratio of $\pi^0(\eta)$ meson production to direct photon production in pp collisions at $\sqrt{s}$ = 200 GeV, generated with PYTHIA under various conditions: (Top) limiting only the transverse momentum of the detected particle, 10 < p_T < 20 GeV/c; (Middle) after application of conditions including an isolation cut described in the text; (Bottom) after additional application of direct meson suppression from the SMD detector. For the purposes of this simulation, the SMD was placed after the fifth layer of the calorimeter, and the same type of SMD (see Fig. 9) was assumed for both barrel and endcap.*

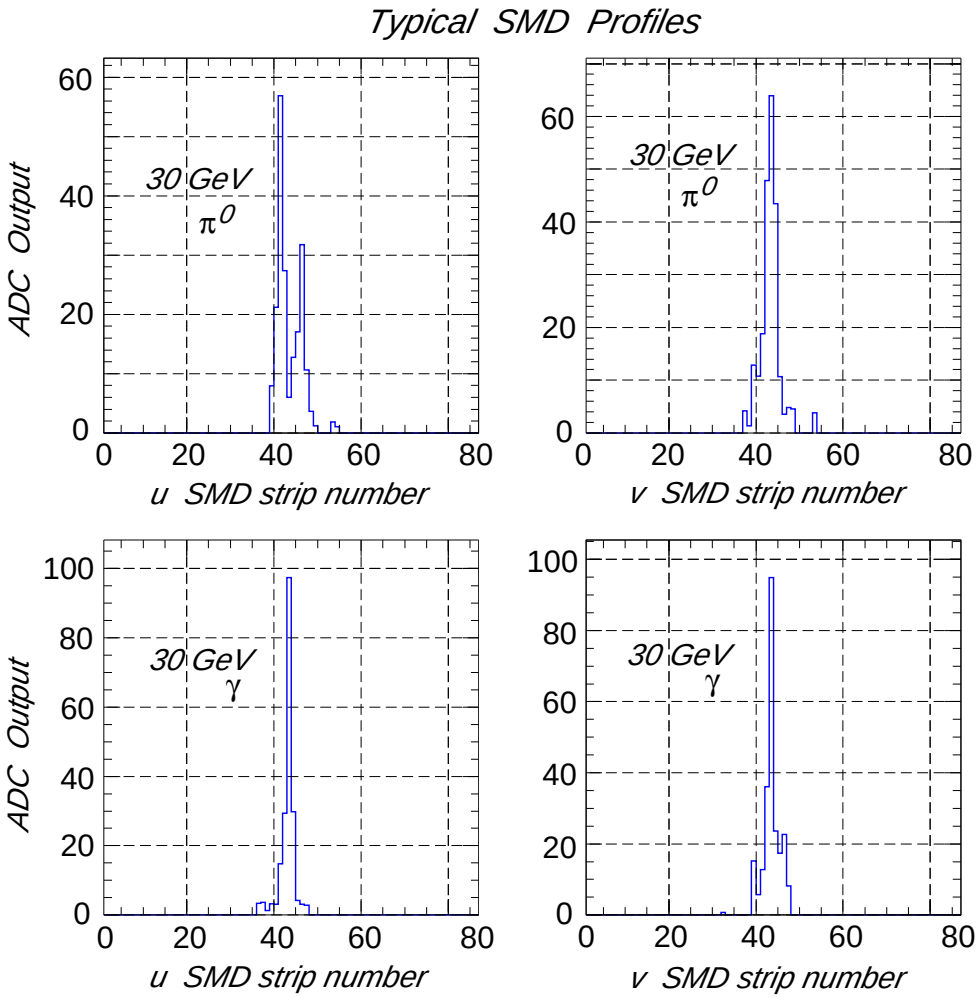

Figure 16: *Comparison of the simulated response of the SMD to a typical 30-GeV direct photon (below) and to a 30-GeV* π^0. *The presence of the second peak in the SMD response clearly indicates two closely spaced photons intercepted by the detector.*

(see Appendix Sec. A.3.2 for details) based on the goodness of fit to the measured response with an adjustable function characteristic of the average response to single photons. This approach rejects ≈80% of the simulated 30-GeV $\pi^0(\eta)$ events, at the expense of ≈20% loss of single photons, a performance comparable to that achieved in experiments with the best existing collider detectors [49]. The best simulated discrimination is provided by a SMD built from two orthogonal planes of overlapping scintillator strips having a triangular cross section, as illustrated in Fig. 9. This design, developed as a preshower detector for the upgrade of the D0 calorimeter [34], stabilizes the lineshape of the transverse profile of the electromagnetic shower, by virtue of the sharing of energy loss between adjacent detector strips. With this design, the simulated background:signal ratio in STAR, after application of isolation and SMD cuts, is reduced to 0.6–0.8, with relatively little dependence on pseudorapidity, as shown in the last frame of Fig. 15. This background level is consistent with *running* experience with the CDF detector [49] at FNAL, if we allow for extrapolation downward to the RHIC energies.

It is important to evaluate the effect of subtracting the remaining background contributions on the precision of information that can be extracted about the gluon polarization. Most of the information needed for this subtraction can be based on *measured* quantities, namely, on the yields (N^{pass}, N^{fail}) and spin correlation asymmetries (A_{LL}^{pass}, A_{LL}^{fail}) for those event samples that pass all cuts and that fail the final SMD cut. The only other quantity needed that is not directly measured is the probability P_m that a meson that passes all other cuts will also survive the SMD cut. In terms of these quantities, within each desired bin, the spin correlation associated with direct photon production can be extracted as follows:

$$A_{LL}^{\gamma} \;=\; A_{LL}^{pass} \;+\; \frac{(A_{LL}^{pass} - A_{LL}^{fail})}{[(\frac{N^{pass}}{N^{fail}})(P_m^{-1} - 1) - 1]}. \qquad (4)$$

This equation assumes that A_{LL}^{pass} and A_{LL}^{fail} differ only because of the different mix of photon and meson events within the two samples; A_{LL}^{γ} and A_{LL}^{meson} must each have the same value within both samples, because neither the decay of spinless mesons nor the shower fluctuations can be influenced by the initial spin state of the proton beams. Our estimates of background subtraction errors in the simulated A_{LL} results, discussed further in Sec. 3.6.1, are based on the above equation, with the values and statistical uncertainties of the four measured quantities determined by the simulations and an assumed uncertainty of ±15% in P_m (i.e., $P_m \approx 0.20 \pm 0.03$ for the present simulations).

The meson SMD survival probability P_m can be extracted from simulations that have been tuned to reproduce the observed variation in the ratio N^{pass}/N^{fail} as the SMD cut is changed. It can also be constrained independently via the observed conversion probabilities in the preshower detector, within the pass and fail event samples. The preshower detector is a scintillator with good light output positioned after about one radiation length of absorber. This early in the stack, there is a considerably greater (and easily simulated) probability of conversion for (at least one of) the pair of photons from meson decay than for a single photon. Hence, the fraction of events in the pass and fail samples that are accompanied by a preshower signal is sensitive to the balance among photons and mesons within each sample. The importance of this crosscheck is likely to grow with increasing photon energy, as the discrimination power of the SMD diminishes. The above constraints appear sufficient to attain at least the assumed uncertainty of ±15% in P_m.

In $\vec{p}\vec{p}$ collisions at $\sqrt{s} = 500$ GeV, there is substantial physics interest in events with direct photons of energy above 50 GeV. This sample includes nearly all the direct photon production

events corresponding to $x_{gluon} > 0.05$, and thus provides overlap in gluon polarization sensitivity with the $\sqrt{s} = 200$ GeV data. The overlap region will allow a powerful crosscheck on model assumptions made in extracting $\Delta G(x, Q^2)$ from the data, and may provide information on the evolution of the spin-dependent gluon distribution. The SMD will provide very limited $\gamma - \pi^0$ discrimination power at such high photon energies. While our simulations suggest (see Appendix) a ratio $(\pi^0 + \eta^0)/\gamma \lesssim 1$ even *without* SMD cuts at the relevant values $p_T > 20$ GeV/c, it is clear from the above discussion that the background subtraction still relies on producing two event samples with significantly different meson-to-photon enrichments. For $E_\gamma > 50$ GeV, the *pass* and *fail* samples discussed above are likely to be replaced by *preshower no* and *preshower yes* samples.

3.4 Electron/Hadron Separation

The production of intermediate vector bosons will be signalled by detection of electrons and positrons at high p_T. Since the STAR detector does not provide good particle identification, the most important background for these weak signals arises from the abundant yields of charged hadrons at high p_T. As indicated by the simulated spectra in Fig. 17, the raw expected signal:background ratio within the STAR acceptance is only of order 1:30, even at the peak of the expected W decay spectrum. However, simple cuts, together with the selective response of the EMC's, appear capable of suppressing the hadronic background by several orders of magnitude, with minimal loss of W's. As illustrated in Fig. 17, one order of magnitude is gained by application of the same isolation cut discussed above for photons. A comparable, independent gain arises from a cut demanding large *missing* p_T in the event, as expected for the neutrino from W decay. The latter cut is more strictly a dijet rejection criterion, discarding events in which the $e^{\pm}$ candidate (at azimuthal angle ϕ) is accompanied by a jet with $p_T > 5$ GeV/c centered in the region $(\phi + \pi - 1, \phi + \pi + 1)$.

Additional hadron suppression is provided by the calorimeter response. The spectra in Fig. 17 are plotted against the *generated* p_T value, rather than against the transverse energy E_T that would actually be measured in the EMC. As illustrated in Fig. 12, for given p_T, the measured E_T is systematically smaller for hadrons than for electrons, so that the *observed* spectra will already be much more favorable than shown in Fig. 17. Over the η range where the TPC provides good momentum resolution, further hadron suppression can be gained by demanding a strong correlation between p_T measured in the TPC and E_T measured in the EMC, as indicated by the diagonal line in Fig. 12. Additional discrimination, applicable even for $\eta \gtrsim 1.5$, where the TPC resolution is substantially deteriorated, can be based on the ratio of energy depositions in the SMD *vs.* total calorimeter depth. The combination of these conditions based on EMC response should lead to at least another order of magnitude gain in $e^{\pm}/h^{\pm}$ ratio.

With all of the above cuts implemented, $W^{\pm}$ production should dominate over charged hadron production throughout the region $E_T \gtrsim 25$ GeV/c. It is important to distinguish the W's clearly over a range of E_T, because the Bjorken x-values of the colliding partons can be determined event-by-event from the combination of E_T and η of the detected $e^{\pm}$.

3.5 Effects of TPC Resolution Deterioration at $\eta > 1$

While the active volume of STAR's TPC nominally extends over the range $-2 \leq \eta \leq +2$, the achievable momentum resolution deteriorates rapidly for tracks at $|\eta| > 1$. The natural reduction

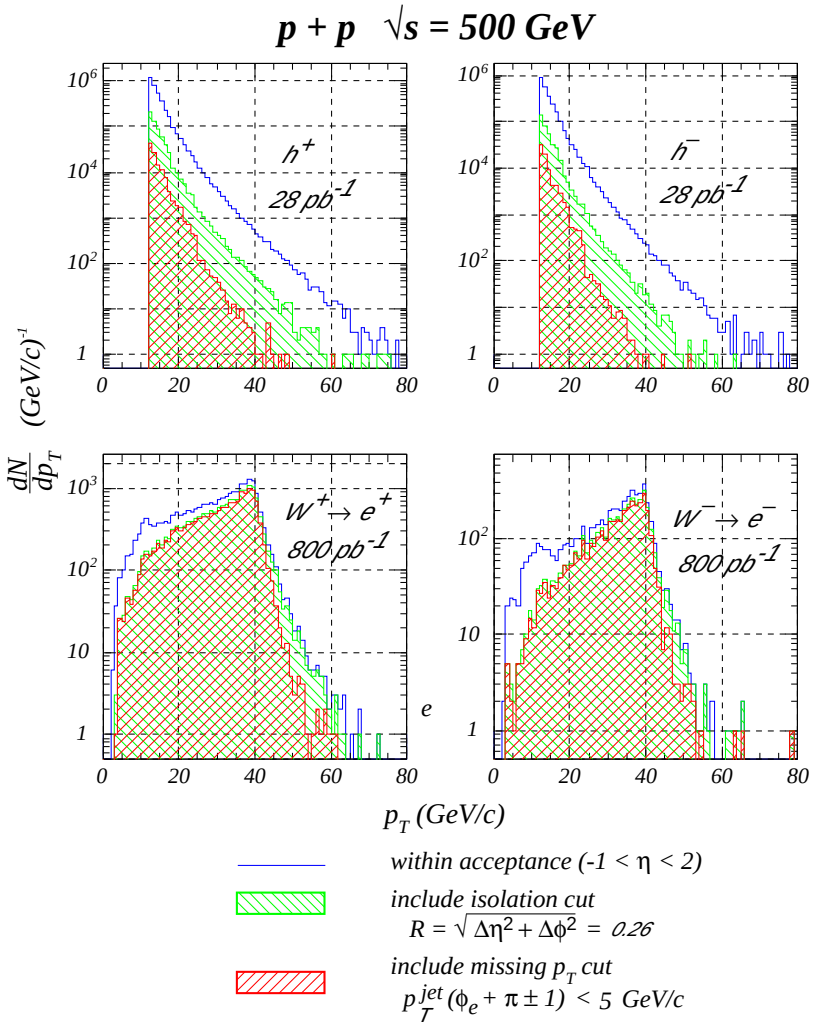

Figure 17: *Simulated (with PYTHIA) p_T spectra for positive and negative hadrons and for positrons and electrons from $W^{\pm}$ decay falling within the STAR + EEMC acceptance for $\sqrt{s}$=500 GeV pp collisions. The hadron spectra correspond to an integrated luminosity of 28 pb^{-1} (with a p_T cutoff of 10 GeV/c imposed in the simulations), while the W decays correspond to 800 pb^{-1}. The included hadrons are p, K^+, π^+, and e^+ from π^0 Dalitz decay, or their antiparticles. The hadron yields are plotted against the* generated *values of p_T, rather than against the smaller transverse energies that would be measured for them in the EMC's. The shaded and cross-hatched spectra show the results of applying first an isolation cut and then a missing p_T cut to the events, as described in the text. These two cuts leave a signal/background ratio of ≈ 1:2 for W^+ and 1:3 for W^- production at $p_T \approx 30$ GeV, which can be improved by a further 1-2 orders of magnitude by cuts associated with the EMC response.*

in the length of the projection of such tracks onto the end planes of the TPC is exacerbated by the sparse layout of readout pads in those end planes, over the innermost half of the radial range spanned. A further problem arises because trigger delays in opening the gate for TPC readout result in a loss of hits for several cm of track nearest the TPC ends. The curvature of tracks at $\eta > 1$ must thus be determined from a significantly reduced set of recorded hits. Assuming that event vertices can still be defined well from associated tracks at $|\eta| < 1$, our simulations (see Appendix) indicate that p_T resolution for individual tracks gets worse by nearly a factor of two for each 0.2 unit increase in η beyond $\eta = 1$.

Surprisingly, the impact of this TPC resolution problem on the physics program we have outlined for the EEMC is not large. We have in any case considered only those jets whose central axis lies at $\eta \leq 1.3$ (in order that they be fully contained within the EEMC acceptance). Thus, the serious TPC resolution deterioration affects mainly softer particles near the outer edge of the considered jet cones. While the charged hadron contribution to the overall jet momentum resolution grows poorer in the endcap region, it remains dominated by the fundamental spread in associating jet momentum with a single parent parton. For the purpose of distinguishing hard photons from electrons or positrons, we need only to have TPC track stubs for the latter particles, not a good momentum determination. The TPC resolution will impose an effective (yet to be simulated) limit on the η values at which high-p_T Λ's can be successfully reconstructed in STAR, but a suitable range for the determination of spin-dependent fragmentation functions [31] is likely to remain.

The most serious impact of the TPC resolution problems will be encountered in the $W^{\pm}$ production experiments, where we must deal with the most rigid charged products. The electron/hadron discrimination cut indicated in Fig. 12 will become ineffective beyond $\eta \approx 1.4$ for the $p_T \geq 25$ GeV/c particles of interest. But the other cuts described in the preceding subsection will probably still permit observation of a clear W signal in this region. On the other hand, we rely on the TPC to distinguish W^+ from W^- production. In the endcap region the charge assignment can be made on the basis of determining χ^2 values for fits to the relevant TPC track with the two possible signs, but with the p_T value deduced from the EEMC measurement. The fits can be further constrained by additional hits derived from the SMD position (where simulated shower centroids are extracted with a resolution $\sigma \approx 2.5$ mm) and from the event vertex (which can be reconstructed in more than 90% of the simulated W production events from TPC tracks for two or more associated charged products with momenta $\gtrsim$400 MeV/c). Ambiguous events, for which the comparison of χ^2 values does not establish a clear $e^{\pm}$ preference, will be excluded from the analyzed sample, leading to an inefficiency that grows with increasing η. The largest-η point included in the simulations in Fig. 6 will probably be inacessible (at least for separated W^+ and W^- analysis), while the error bar on the next point will grow by a factor of 1.5–2. The errors on points in the range $1.0 \leq \eta \leq 1.4$ will be only slightly affected by this sign ambiguity.

We are beginning to explore possible methods for alleviating the TPC resolution problem for W production. One possibility involves moving the colliding beam interaction diamond further away from the endcap, to increase the track projection length at given η, as well as to bring some SVT hits to bear. The feasibility of such a change, and its impact on other aspects of the physics program, have yet to be assessed.

3.6 Extraction of Polarized Parton Distribution Functions

3.6.1 $\Delta G(x)$

Uncertainties in the gluon polarization information extracted from STAR experiments are likely to be dominated by systematic, rather than statistical errors. Some of the systematic uncertainties are associated with the procedures used to analyze the data to extract $\Delta G(x_g, Q^2)$. We have performed simulations to begin to assess these uncertainties.

The ultimate extraction of ΔG is likely to be made by including RHIC polarization data, along with the polarized deep inelastic scattering data base, in global theoretical fits carried out at next-to-leading order (NLO) in QCD. However, analogous treatments of unpolarized gluon distributions have made clear [8, 9] that there are a number of theoretical ambiguities that must be constrained, over and above poorly known parton distributions and helicities. These include NLO contributions, theoretical scale ambiguities [9], proper treatment of isolation cuts and jet definitions, and the effect of initial *transverse* momenta of the colliding partons [8] (called "k_T smearing effects"). We expect the best overall constraints on $\Delta G(x_g, Q^2)$ to come from experiments that approach most closely the ideal of a direct leading-order extraction at experimentally determined x_g values.

We have applied such a direct extraction algorithm to simulated photon production data. The simulations do not yet include NLO contributions (known to be small [12]) to the photon production mechanism, but they do include *all* leading-order contributions, as well as initial-state radiation that introduces substantial k_T smearing prior to the hard parton-parton collision. Polarization effects are included in the simulations by determining the probability that each event generated by PYTHIA would have arisen from parallel *vs.* antiparallel orientations of the two beam spins, and then choosing the spin state randomly in accord with those probabilities. The probabilities are based on leading-order QCD predictions [11] for the partonic spin correlations $\hat{a}_{LL}(\theta^*)$ and Gehrmann-Stirling [6] parton helicity distributions $\Delta q(x_q, Q^2)$, $\Delta G(x_g, Q^2)$, evaluated at the c.m. angle, x_q, x_g values and $Q^2 = p_T^2/2$ of the generated hard parton-parton collision. The probabilities are calculated assuming a polarization of 0.7 for each beam.

In contrast, the event reconstruction algorithm applied to the simulated data was simple-minded: all events were assumed to arise from the gluon Compton scattering process alone, with $k_T = 0$ and $x_g = \min[x_1, x_2]$, dictating the choice of sign for $\cos\theta^*$. The reconstructed events were subjected to cuts foreseen for the analysis of real data. These included isolation and SMD cuts needed to suppress mesonic background, but also other cuts expected to reduce certain systematic errors. The photon was required to have a minimum p_T of 10 GeV/c, thought to be necessary to limit higher-twist effects and thus guarantee applicability of perturbative QCD. The larger of the two reconstructed x-values was required to exceed 0.20, in order to emphasize asymmetric parton collisions with the largest quark polarization and least ambiguity in assigning $x_{1(2)}$ to quark *vs.* gluon. The simplifying assumptions of the analysis allow us to extract the gluon helicity preference within each bin of reconstructed x_g values as follows:

$$\Delta G(x_g) \;=\; \frac{[N_{++}(x_g) - N_{+-}(x_g)]}{P_{b_1} P_{b_2} \sum_{i=1}^{N_{++}+N_{+-}} [A_{1_p}^{\rm DIS}(x_{q_i}, Q_i^2)\hat{a}_{LL}^{\rm Compton}(\cos\theta_i^*)/G(x_{g_i}, Q_i^2)]}, \qquad (5)$$

where $N_{++(+-)}$ represent the simulated yields with equal (opposite) proton helicities and $P_{b_{1(2)}}$ the proton beam polarizations. The product of the deep inelastic scattering (DIS) asymmetry A_{1_p} (which measures the quark polarization) and the Compton subprocess spin correlation,

divided by the *unpolarized* evolved gluon distribution function, is accumulated over all events, in order to determine the average sensitivity to $\Delta G(x_g)$ within the given x_g bin. The evolution of A_{1_p} with Q^2 depends, in principle, on the unknown $\Delta G(x, Q^2)$, necessitating an iterative approach to self-consistency in the application of eq. (5). However, this effect is minimal in practice with the restriction to large x_q-values [6].

The results of the simulation and simplified data analysis at $\sqrt{s}$=200 GeV are shown in Fig. 4. The *extracted* $\Delta G(x_g)$ is compared to the theoretical input (Gehrmann-Stirling model A [6], evolved to the most probable value Q^2=50 (GeV/c)^2), which is consistent with observed scaling violations in polarized DIS. The systematic discrepancy seen at $x_g > 0.1$ in Fig. 4 reflects the simplifying assumptions of the analysis. In particular, the generated contributions from $q\overline{q} \to g\gamma$ and from the Compton process with $x_g > x_q$ both tend to yield an underestimate of $\Delta G(x)$ when they are neglected in the analysis. The finite experimental resolution in reconstructing θ_i^* also contributes to the discrepancy, since $\hat{a}_{LL}^{\rm Compton}$ is not a linear function of θ^*. Error contributions from k_T smearing are far smaller than in the analysis of *unpolarized* gluon distributions [8]. The reduced sensitivity to k_T comes from two compensating effects. A non-zero average value of k_T leads to an over- or underestimate of p_T, and hence, via eq. (2), to correlated errors in the extracted values for x_g and x_q. A systematic overestimate (for example) of x_{q_i} and of x_{g_i} on the right-hand side of eq. (5) leads to an underestimate of $\Delta G(x)$. But then that underestimated value is plotted at too large an x_g value. Since $\Delta G(x)$ is a monotonically decreasing function for $x_g \geq 0.01$ (for all three Gehrmann-Stirling models shown in Fig. 2), the net effect of k_T is to move data *along* the curve, rather than above or below it.

The net systematic deviation in the directly extracted values of $\Delta G(x)$ in Fig. 4 is $\sim 30\%$ in the worst x_g bins, and is much smaller in the *integral* ΔG that would be deduced from these data. The *model-dependence* introduced by correcting these deviations via simulations is likely to be less than half the size of the corrections themselves. The fact that $\Delta G(x)$ can be extracted directly from photon-jet coincidence events in STAR, with small model-dependence, suggests that STAR data will be definitive in tying down the gluon polarization in more sophisticated global analyses. This is especially true in the critical region $x_g < 0.1$, where the endcap acceptance is essential and the simple analysis described above is most successful.

Measurements at 200 GeV will provide useful information only down to $x_g^{min} \approx 0.04$. The range will be extended further downward to $x_g^{min} \approx 0.01$ by runs at 500 GeV, as illustrated in Fig. 18. This extension is critical for constraining the extrapolation of $\Delta G(x)$ toward $x_g = 0$, in order to evaluate the integrated gluon contribution to the proton's helicity. However, it will be important to get experience at 200 GeV before attempting a 500 GeV measurement, because several experimental challenges become more demanding at the higher energy. For example, at full luminosity one would have to deal with about four times as many TPC pileup tracks at 500 GeV. Furthermore, at lower x_g values, the expected reductions in gluon polarization will lead to smaller measured asymmetries, hence greater sensitivity to potential instrumental asymmetries in the apparatus. An important feature of 500 GeV measurements is that the gluon polarization can still be probed with significant statistical precision at $x_g \gtrsim 0.05$, in events characterized by $p_T > 20$ GeV/c (see Fig. 18). At these higher p_T values, it is expected that the yield of π^0's will decrease much more rapidly than that of γ's, compensating for the diminished capability of the SMD to distinguish between them. The comparison of 200 and 500 GeV results within overlapping x_g regions can provide information on the Q^2-evolution of $\Delta G(x)$, as well as a powerful crosscheck on both experimental and theoretical systematic uncertainties.

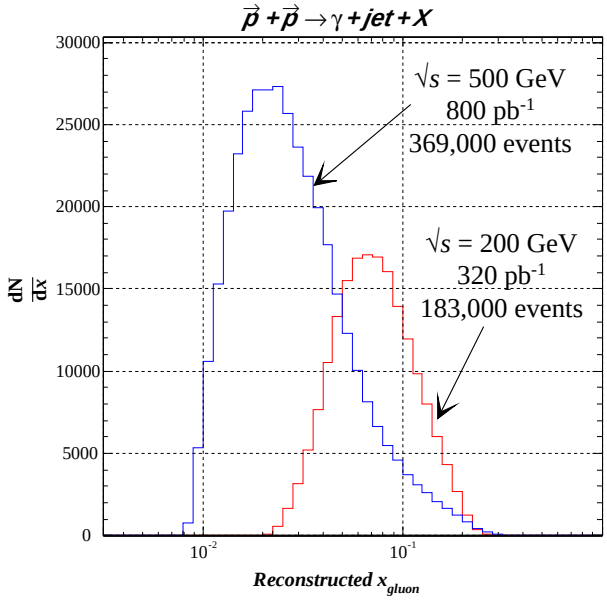

Figure 18: *Distribution of simulated direct-photon events versus the reconstructed gluon momentum fraction for $\sqrt{s}$ = 200 and 500 GeV pp collisions, at respective integrated luminosities of 320 and 800 pb^{-1}. The 500 GeV simulation includes no upper cutoff on p_T, while the 200 GeV simulation includes only events with p_T < 20 GeV/c. (At both energies, a minimum p_T of 10 GeV/c and a minimum x_{quark} of 0.20 were imposed.) If p_T < 20 GeV/c were imposed on the 500 GeV results, there would be very little overlap region in x_{gluon} between the two energies.*

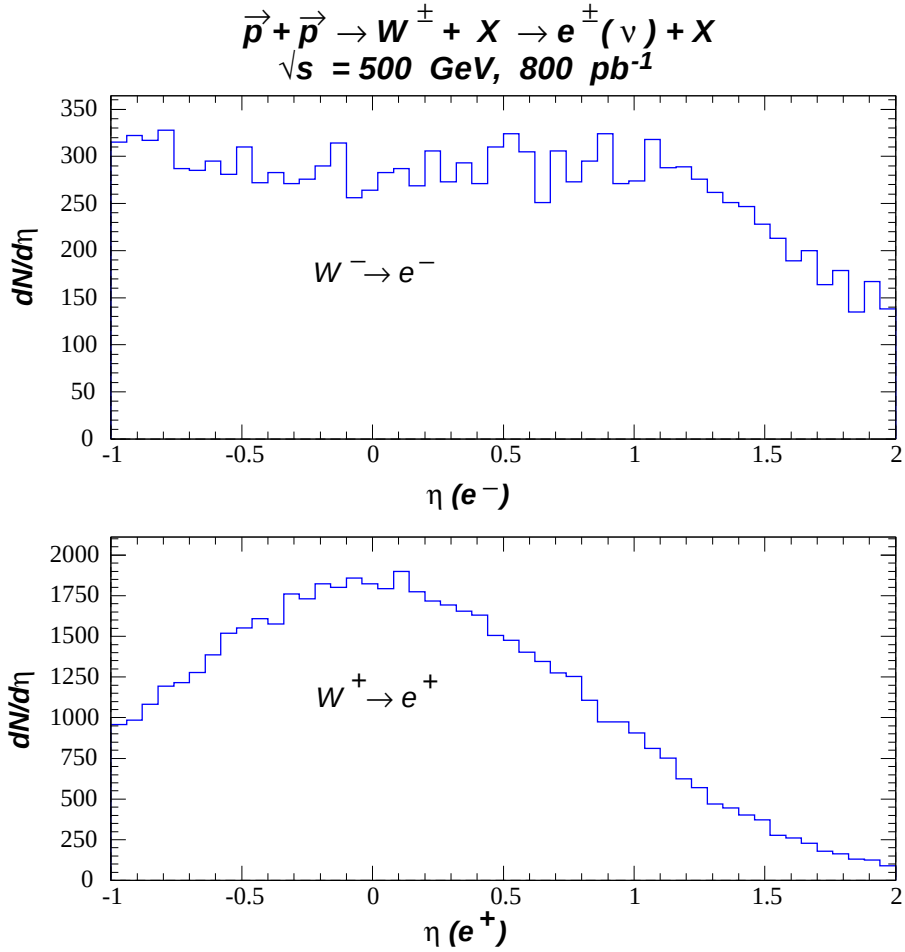

Figure 19: *Simulated pseudorapidity distribution of electrons (positrons) from $W^-(W^+)$ decays, produced by $\sqrt{s}$ = 500 GeV pp collisions.*

3.6.2 $\Delta\overline{q}(x)$

The yields of $W^{\pm}$ production are sufficient for a meaningful extraction of antiquark helicity distributions only at the highest RHIC energy ($\sqrt{s}$ = 500 GeV). Information on four different spin-dependent structure functions – $\Delta u(x)$, $\Delta d(x)$, $\Delta\overline{d}(x)$ and $\Delta\overline{u}(x)$ – will be obtained from four measured quantities: the single-spin longitudinal analyzing powers $A_L^{(a)}$ and $A_L^{(b)}$, sensitive to helicity flip of proton beams a and b, respectively, for W^+ and W^- production. These analyzing powers are given directly in terms of the structure functions; e.g.,

$$A_L^{(a)}(W^-) = \frac{\Delta d(x_a)\overline{u}(x_b) - \Delta\overline{u}(x_a)d(x_b)}{d(x_a)\overline{u}(x_b) + \overline{u}(x_a)d(x_b)}, \quad (6)$$

$$A_L^{(b)}(W^-) = \frac{d(x_a)\Delta\overline{u}(x_b) - \overline{u}(x_a)\Delta d(x_b)}{d(x_a)\overline{u}(x_b) + \overline{u}(x_a)d(x_b)}, \quad (7)$$

where we have neglected contributions from heavier flavors. The results for W^+ can be obtained

from those above by the substitutions $d \to u$, $\overline{u} \to \overline{d}$. The subscripts on x-values in these expressions label the proton from which the designated parton originates.

In general, the above analyzing powers have significant contributions from *both* quark and antiquark helicities. But the situation simplifies considerably for asymmetric collisions with $x_a >> x_b$, as are selectively probed by the endcap for W^- production. Then, the known *unpolarized* structure functions suggest that:

$$A_L^{(a)}(W^-, x_a >> x_b) \approx \frac{\Delta d(x_a)}{d(x_a)}; \tag{8}$$

$$A_L^{(b)}(W^-, x_a >> x_b) \approx \frac{\Delta \overline{u}(x_b)}{\overline{u}(x_b)} - \frac{\overline{u}(x_a)\Delta d(x_b)}{d(x_a)\overline{u}(x_b)}. \tag{9}$$

The separation evident in the latter equations allows one to approach a direct extraction of antiquark polarizations at low x, and furthermore to calibrate the use of $W^\pm$ production by seeing if the results reproduce DIS measurements of quark polarization at $x \gtrsim 0.2$.

Event-by-event reconstruction of $x_{a(b)}$ values is more complicated than in the photon production case, since one detects the W's only via their $e^\pm$ decay daughters, and without any kinematic coincidence. Because the W is produced as an s-channel resonance in the partonic c.m. frame, it is nonetheless possible (with reduced resolution) to deduce the x-values from the combination of η and p_T measurements for the $e^\pm$. The η-distributions expected, and the correlations between η and x_q, $x_{\overline{q}}$, are quite different for W^+ *vs.* W^-, as illustrated by simulated data in Figs. 19 and 20. For example, 98% of the W^- daughters detected in the endcap region arise from fusion of a d quark from beam a (the beam headed toward the endcap) with a $\overline{u}$ from beam b. For these events $A_L^{(a)}$ provides a direct determination of $\Delta d(x_a)/d(x_a)$ over the approximate range $0.1 < x_a < 0.5$, and $A_L^{(b)}$ of $\Delta\overline{u}(x_b)/\overline{u}(x_b)$ over the range $0.05 < x_b < 0.15$ (see Fig. 20). The statistical uncertainties attainable are indicated by the simulation results in Fig. 6, subject to the caveats introduced in Sec. 3.5. The value of $A_L^{(b)}(W^-)$ in the endcap region is near zero in Fig. 6 only because the Gehrmann-Stirling [6] helicity distributions used in the simulations happen to give essentially unpolarized $\overline{u}$ quarks in the relevant x range.

The separation of quark and antiquark helicity sensitivities is not as clean for W^+ production, because the e^+ is emitted most often opposite the W^+ direction. As seen in Fig. 20, events with W^+ daughters in the endcap encompass sizable contributions from collisions with $x_a \approx x_b$, as well as with $x_a >> x_b$. For events in the former category, beam a provides the $\overline{d}$ preferentially, while for the latter it provides the u quark. We are currently exploring whether the $x_{a(b)}$ reconstruction resolution will be sufficient to exploit this difference for a reasonably accurate extraction of the separate spin structure functions from these W^+ production events.

3.7 Energy Calibration

Systematic errors in the x-values reconstructed for the colliding partons, *e.g.*, via eq. (2), give rise to systematic errors in the extracted spin structure information. The reliance of the x-values on p_T measurements for photons or very energetic $e^\pm$ (where the TPC resolution is limited) thus places a high premium on the absolute energy calibration of the EMC response. We have assessed the accuracy level needed by reanalyzing the simulated photon-jet coincidence events with the introduction of a $\pm 5\%$ miscalibration of the EEMC energy scale. We have then fitted the extracted $\Delta G(x)$ values, like those in Fig. 4, with the functional form used in

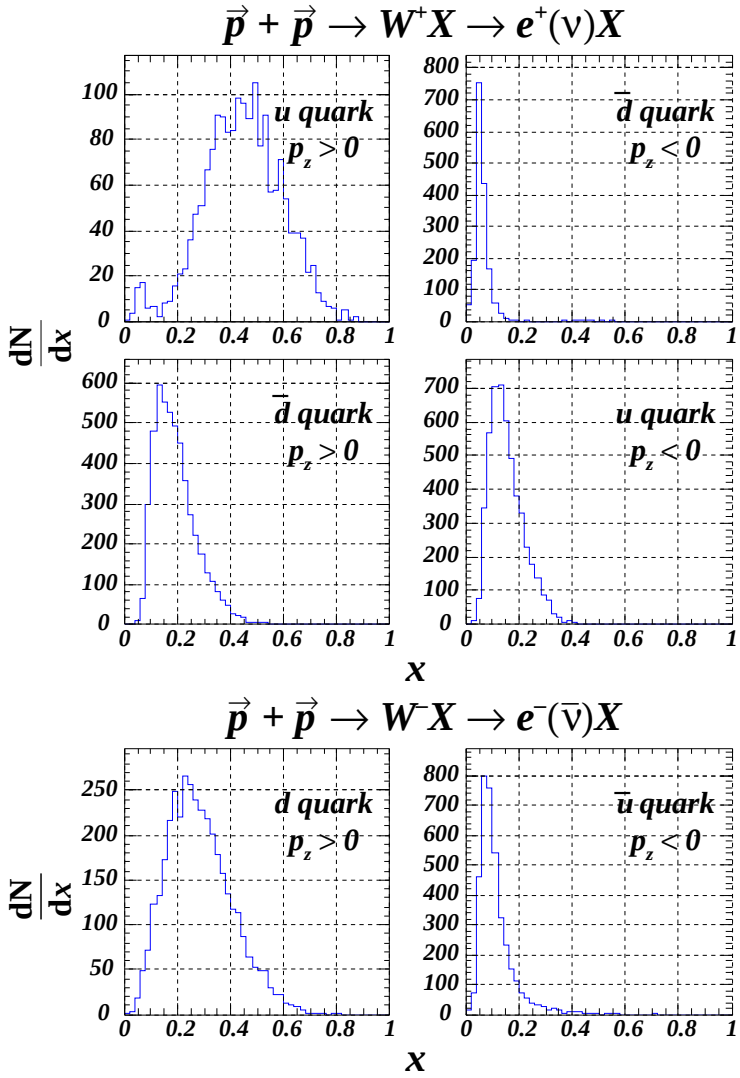

Figure 20: *The distribution of x-values for quarks and antiquarks probed by $W^{\pm}$ production yielding $e^{\pm}$ in the EMC endcap. In the W^- case, beam a yields the d quark and beam b the $\overline{u}$ 98% of the time, so the distributions for the alternative assignment are not shown. Results for both contributions are shown for W^+. The differences between $W^{\pm}$ results arise because the W is produced left-handed in each case, leading to preferential emission of electrons (positrons) parallel (antiparallel) to the W^- (W^+) direction.*

the Gerhmann-Stirling [6] curves in Fig. 2. This procedure allows us to evaluate the effect of miscalibration on the inferred integral ΔG. When simulated results from both 200 and 500 GeV runs are included, a 5% miscalibration introduces a $\approx 10\%$ change in the integral. Thus, in order to keep the energy calibration effect smaller than the (probably dominant) $\pm 10\%$ systematic error expected from the absolute calibration of the beam polarization at RHIC, it is important to plan for an energy calibration to $\pm 2 - 3\%$. The measurement of differential cross sections falling rapidly with increasing p_T imposes a similar limit [36].

The calibration requirement is not beyond the state of the art for similar calorimeters, which seems to be $\approx 1\%$ [47, 49]. However, it has significant implications for electronics and run procedures. It is extremely useful for calibration purposes to keep the peak for minimum-ionizing particles (which will deposit ~ 15 MeV in a typical tower) within the spectrum for each tower during data-taking. This requires a minimum of 12-bit ADC ranges for the towers. Calibration points at higher energies can be provided during STAR data acquisition by tying the EEMC response for electrons and positrons to the corresponding momenta measured in the TPC. However, the deteriorating TPC resolution will impose an η-dependent upper limit on the p_T values at which such cross-calibrations can be effectively performed (*e.g.*, ≈ 10 GeV/c for $\eta = 1.5$). Calibrations above this effective limit can be accomplished by reconstructing correct invariant masses for decays such as $J/\Psi \to e^+e^-$, $\rho^\pm \to \pi^\pm\pi^0$ and $Z^0 \to e^+e^-$, where the momentum of the coincident decay daughter can be measured well by the TPC or by otherwise calibrated portions of the EMC. Some of these decay calibrations might require dedicated running with specialized triggers. In addition to these calibrations *during* production running, it is clearly important, via cosmic ray and test beam results, to provide a sufficiently good calibration *beforehand* to set the ADC range and trigger thresholds appropriately. Transfer of test-beam calibrations to the final calorimeter configuration will require incorporation of some form of radioactive source or light-pulsing system within the EEMC. The details of all these calibration needs are under continuing study.

Calibration points over a very wide range of pulse heights will be needed to establish the linearity of the calorimeter response over the range of energies needed for the physics program. This range runs from few hundred MeV photons from asymmetric π^0 decays (also needed to monitor few percent leakage of 10 GeV photon showers into neighboring calorimeter towers) through 150 GeV electrons ($p_T = 40$ GeV/c at $\eta = 2$) from W^- decay. The simulation results in Fig. 11 demonstrate at least that the calorimeter design yields a quite linear response over the energy range of interest for direct photon production at 200 GeV. The high degree of linearity observed in Fig. 11, for events spanning the entire area of the endcap, arises in part from compensating dependences of the sampling fraction on photon energy and on angle of incidence. We will have to make corrections for expected nonlinearities at higher energies, arising from shower leakage out the back of the EEMC ($\approx 8\%$ at 150 GeV and $\eta = 2$). Of course, nonlinearities can be introduced as well by gain mismatches among different scintillating tiles within a given tower or in the electronics, and these effects have been neglected in the simulations to date.

3.8 Beam Polarization and Luminosity Monitoring

Important sources of systematic error in the determination of spin structure functions at RHIC are associated with the accuracy of online monitoring of the beam polarizations and of the relative integrated luminosity for different combinations of beam spin orientations. For example, the polarization of each beam must eventually be determined with $\pm 5\%$ absolute accuracy in

order to limit the normalization uncertainty on extracted values of $\Delta G(x_g, Q^2)$ to $\pm 10\%$. These issues are being addressed by collaborators on both the PHENIX and STAR detectors.

Polarimeters allowing a rapid, reliable, and precise determination of the beam polarizations require reactions at the appropriate beam energies that have known large yields and analyzing powers. The available data at RHIC energies are sparse and, except for inclusive $\pi^{\pm}$ production in pp collisions at 200 GeV/c on a fixed target [50], are not known to anywhere close to the required precision. Thus, calibration schemes must be built into design of RHIC polarimeters.

Commissioning of the polarized beam at RHIC will likely involve polarimeters based on $\pi^{\pm}$ production (recently measured [51] at RHIC injection energy using a carbon target), or elastic scattering from carbon in the Coulomb-nuclear interference (CNI) region. The analyzing power of the latter process can be predicted semiquantitatively from the combination of the known spin-flip electromagnetic amplitude with spin-independent pomeron exchange [52]. However, this analyzing power is quite small, so that a CNI polarimeter may be subject to significant systematic errors. Production running at RHIC will require polarization monitoring that involves simple detector schemes with a high spin sensitivity (to reduce systematic errors) located near each intersection region, so that the proper operation of the spin rotation system may be verified. Other processes, such as $pn \to np$ charge exchange scattering on neutrons in a nuclear target, need investigation at RHIC energies, since the absence of the usually dominant spin-independent pomeron-exchange amplitude, together with lower-energy measurements [53], suggest that large spin effects may be present. In any case, the polarimeters would be calibrated against the polarization of a fixed, internal proton target at some other location within RHIC, exploiting the indistinguishability of the beam and target protons in measurements of one of the above strongly spin-dependent processes. The development of RHIC polarimetry is a major project on its own, but the 5% absolute accuracy goal should be attainable.

Relative normalization of the spin parallel and anti-parallel reaction rates requires a monitor of the luminosity for each state that has a high rate (for statistical precision) and a vanishing (or well known) sensitivity to the beam polarizations. Candidates include minimum bias triggers from various parts of the STAR detector, including the zero degree calorimeters (not shown in Fig. 7). Checking for spin insensitivity will involve comparisons among various candidate trigger rates, with the expectation that the lowest spin sensitivity will be associated with low p_T events [54]. This is likely to converge to a satisfactory level, since it is already known that the sensitivity of the total cross section to spin, $\Delta\sigma_L$, is smaller than the pp reaction cross section by more than 3 orders of magnitude in the RHIC energy range [55].

4 Budget, Management, Responsibilities and Timeline

4.1 Budget

A very preliminary outline of the budget for the endcap calorimeter project is shown in the table following on the next page. It is intended to give an indication of the approximate magnitude of the project in its various parts as understood at this stage. A breakdown into equipment and labor (in units of \$1 K) is given for: the converter/scintillator assembly with its fiber/PMT readout (including the preshower detector PMT's and readout); the front end electronics, trigger and DAQ components; the controls and conventional systems integrated into the STAR environment; the shower maximum detector (SMD) scintillator-fiber system and associated Multi-Anode PMT readout and electronics. With the exception of the SMD, the listed items track with equivalent

barrel EMC budget lines and have been given the corresponding WBS numbers, as indicated in the first column. The contingency factor estimates (a STAR/DOE manifestation) are at present taken over directly from the barrel. For the NSF, contingency must be "built" in, and for some items, this is already reflected in the base cost estimate as described below.

Broadly speaking, equipment and manpower entries in the table have for many cases been scaled from the equivalent numerical estimates presented for the STAR barrel EMC project at the time of the 5/98 Construction Readiness Review. Where possible, scaled estimates from the CDF plug upgrade are also used. In the latter case, "as built" numbers are being sought, since many of the same construction elements are to be used in the present STAR endcap EMC design. Additionally, some design and cost estimates from STAR Note #120 [38] have been used where applicable. Obviously, we have benefited significantly from the results of all these previous efforts, and the discussions which we have had with STAR EMC barrel colleagues, CDF plug design leaders (Jim Kirby et al.), and Argonne engineers (Tom Fornek and Ed Bielick) and associated physicists who worked on the endcap design in [38].

In our cost breakdown and cost estimation procedures we have generally attempted to follow the STAR guidelines. There are, however, several important caveats to be associated with the budget numbers presented in the table. Many entries are still being evaluated in detail and are likely to change in the near future. This is especially true of the electronics (for the SMD readout, in particular) where the applicability of barrel EMC solutions may not be appropriate and/or the barrel designs are in too early a stage of development to provide reliable cost estimates. For the latter, the rather large contingency shown probably balances a somewhat reduced cost estimate, made on the basis that significant development and prototyping time would be saved in taking over barrel EMC designs. Other clarifications include: the equipment estimates are based for now on domestic and Japanese commercial suppliers for scintillators, fibers and photo-multiplier tubes; a preshower detector is built into the design with MAPMT readout and electronics costs included in the various fiber/scintillator/PMT/electronics WBS lines; labor estimates at present reflect fully loaded university laboratory rates for non-student engineers, draftsmen, technicians, machinists and general laborers.

In summary, we think this account gives a reasonably conservative estimate of the magnitude of the overall endcap EMC construction project in this stage of its development. As such, it also provides a useful guide in planning for the procurement of the total amount of funding required for this effort. Because we think that there can be some savings in labor costs (e.g., by use of student labor) and equipment costs (e.g., by using alternative suppliers), we take in our present planning a number, $\sim$ \$5.5 M, halfway between the estimated "cost" and "cost + contingency" as given in the budget estimate table. We plan to request EEMC construction money from the NSF in two separate new proposals totaling \$4.0 M. One such proposal will be an application for a Major Research Instrumentation (MRI) grant of \$2 M (the maximum available for this kind of NSF award), to be supplemented by \$0.85 M matching funds from Indiana University. This would cover the basic structure and elements of the sampling calorimeter (the first three budget items, including equipment and labor). Separately, we plan to submit an additional 3-year NSF grant request directly to the Physics Division for a total of \$2 M. While the submission and award dates are different for these two separate funding avenues, we plan to submit both proposals in a coordinated manner to the NSF by November 4^{th}, 1998, the NSF target date. For the remainder of the funds needed, up to $\sim$ \$0.65 M, it is anticipated that some part of the labor and perhaps some amount of the equipment costs, yet to be determined, would be paid from the existing IUCF operating budget, and from two smaller accounts held by Indiana

PRELIMINARY ENDCAP BUDGET ESTIMATES -- k$

		EQUIP	LABOR	SUM	w/ CONT
4.5.3.1	Converter Plates/Structure	368	293	619	740
4.5.3.2	Tile-Fiber System	1121	312	1433	1872
4.5.3.3	PhotoMultiplier Tube System	401	55	456	550
4.5.3.4	Calibration Apparatus	125	34	159	199
4.5.3.5	Module Assembly and Tests	106	96	206	250
4.5.3.6	Prototypes	30	11	41	41
4.5.3.8	STAR Installation and Tests	30	131	161	208
4.5.3.9	EMC Front End Electronics	178	109	288	377
4.5.3.10	Contribution to DAQ	16	6	22	27
4.5.3.11	Online System Contribution	7	26	33	42
4.5.3.12	L0 Trigger Contribution	53	3	56	65
4.5.3.13	Endcap EMC Controls	30	13	44	51
4.5.3.15	Endcap EMC Conventional Systems	79	13	92	104
4.5.3.16	Integration and Management	0	186	186	227
4.5.4.1	Shower Max. Det. Scintillator/Fiber System	101	95	196	235
4.5.4.2	Shower Max. Det Prototypes	30	11	41	41
4.5.4.3	Shower Max. MAPMT System	658	48	706	854
4.5.4.4	Shower Max. Electronics	74	70	144	184
4.5.4.5	Shower Max. Conventional Systems	17	8	25	27
	TOTALS	3424	1520	4908	6094

University Faculty. While the above funding scenario suffices to cover the total anticipated EEMC construction project monetary needs, clearly, additional resources from collaborating institutions would greatly help. Such contributions in the form of reduced cost or contributed labor, capability for supplying reduced fabrication or equipment costs, or the possibility of generating additional support by separate grant funds, are actively being pursued with the endcap construction collaborators already on this proposal, as well as those we might be able to attract. We expect the situation to be more clear at the time of the NSF proposal submission date.

4.2 Management of the Construction Project

It is envisioned that Indiana University will be the lead institution in this project, with a group comprising many of the scientific and technical personnel at the Indiana University Cyclotron Facility and members of the Indiana University Physics Department teaching and research faculty. This group has successfully run a large accelerator facility, and a research program with a 50% international and domestic user group base in intermediate energy Nuclear Physics, for over 20 years. However, given the scale of the endcap project, this effort will clearly require substantial contributing effort from collaborating institutions. This subject is dealt with further in the next section of this document.

Management of the endcap EMC construction project and its implementation will be located at Indiana University. Strong support in this construction effort will come from members of the Indiana Nuclear Group, both Teaching and Research Faculty, of which Prof. Steve Vigdor is Scientific Leader for this project.

Dr. Will Jacobs of IUCF will take on the overall management responsibility as Project Director. Dr. Jacobs is the Division Head for Experimental Support at IUCF. In that role, he supervises a professional and technical staff, and has overseen the completion of many detector design/development/construction projects. Dr. Jacobs has had over 25 years of experience in Nuclear Physics research and has been IUCF Division Head since 1988.

Dr. Jim Sowinski will serve as Deputy Project Director. Dr. Sowinski has over 15 years experience in Nuclear Physics, during which time he has been involved with, and been spokesman for, several technically demanding projects. Dr. Sowinski took a sabbatical leave at DESY at the time of the final HERMES installation and initial commissioning and was an active contributor to that effort. Both Drs. Jacobs and Sowinski are members of the Research Faculty at Indiana, and as such have no required classroom teaching duties.

The Indiana University Cyclotron Facility (IUCF) comprises about 70 professional and technical staff who operate/maintain and develop the existing accelerator complex and its experimental facilities. The Facility has been engaged locally in many accelerator and major detector construction projects since its inception and thus has the infrastructure and personnel to lead the endcap EMC construction project. The laboratory has a large machine shop, drafting and engineering capabilities, electronics and controls groups, scintillator and wire chamber labs, etc., providing a wide range of experience to draw from. It also has extensive setup areas for major equipment assembly. At present, the Facility is supported by a NSF grant, including funds for machine operations as well as ongoing research efforts by the Indiana University Nuclear Group. While the NSF has announced plans to terminate funding of accelerator operations for Nuclear Physics at Indiana at the end of FY'01, other planned uses of the accelerator complex (the cyclotrons, high energy beam lines and associated experimental areas) are forging ahead.

A focused Nuclear and Accelerator Physics program is planned on the "Cooler" storage ring for at least another 4 years.

Given the above, IUCF is in a good position to bring many experienced professional and technical personnel to the fore in the endcap construction project. However, such a large project clearly requires the additional collaborative efforts of several other institutions, both for reasons of manpower and expertise.

4.3 Collaborating Institutions and Responsibilities

An internal STAR review of the Endcap EMC proposal was concluded earlier this summer, with approval by the STAR Council and the strong endorsement by the STAR review committee of the STAR spin-physics program it would enable. A separate considerable effort has gone on in parallel with that review, that is, contacting and persuading other groups to join in this proposal as it now moves toward consideration by the BNL/RHIC PAC. As evidenced by the cover sheet of this document, a significant number of collaborators have joined from the many institutions who had previously expressed strong interest in the construction effort and who had supported the physics goals proposed at the time of STAR review.

The institutions with collaborators on board at the time of this writing are:

- Brookhaven National Laboratory
- Dubna (JINR)
- IUCF/Indiana
- Kent State University
- Michigan State University
- Penn State University
- Rice University
- UCLA
- U. Texas at Austin
- Wayne State University.

Members of the many additional substantial collaborating institutions of the barrel EMC project (Argonne National Laboratory and LBL) are, of course, strongly interested in the endcap EMC project and have considerable expertise which we will utilize, whether or not they decide to join the proposal formally. In many instances, technological solutions are common for the two projects. Nonetheless, in addition to both these explicit (and implicit) avenues of support, we are actively soliciting new collaborators, including groups not presently within the STAR collaboration, to join the endcap construction project and the spin physics program that it makes possible.

A preliminary idea of several aspects of the collaborative responsibilities has begun to take shape. Suggested tasks under discussion, in addition to those described for IUCF above, by institution are: BNL – EEMC installation and testing help; Dubna – possible supplier of Tungsten

radiator sheets (to replace the Pb sheets on which the present design is based) and other tasks under discussion; KSU – software support and polarimetry projects; MSU – fiber production; PSU – portion of the front-end electronics; RICE – triggering issues (L3); WSU – online software, physics simulation and analysis. Further details of a task division and sub-project management plan await a more complete delineation of the collaborating institutions and their possible contributions. Obviously, we intend to have the dividion of responsibilities more completely defined by the time of the NSF proposal submission.

4.4 Timeline

The goal of the EMC endcap proposal will be completion of the project in time to install the EEMC in the west end of the STAR detector during the summer break in the running schedule for the year 2002. This overlaps with the timeline for installation of the final modules of the barrel EMC. By that time, polarized proton collisions at the luminosities assumed in this proposal should be available at RHIC, so that the full research program outlined above can be initiated promptly.

Actual construction of the endcap EMC is expected to take place over a three-year time period. Hence three-year funding for this purpose is being sought with an expected approval/starting date of summer 1999. While such a schedule is aggressive, it is one dictated by present funding cycles and not out of scale with the barrel EMC project timeline. Where possible, other resources are being used to pursue detector prototyping and design/engineering issues in advance of the actual funding approval. For example, the IUCF group has just received a \$95 K grant from Indiana University to initiate detector prototyping, detailed engineering design and improved simulations for the endcap project. Prototype tests of extruded scintillator strips for the Shower Maximum Detector are already underway.

While a detailed plan of the construction is not yet in place, several key milestones we envision as necessary to maintain a proper construction schedule are indicated on the accompanying schematic Gantt chart.

PRELIMINARY SCHEDULE MILESTONES FOR THE STAR ENDCAP ELECTROMAGNETIC CALORIMETER

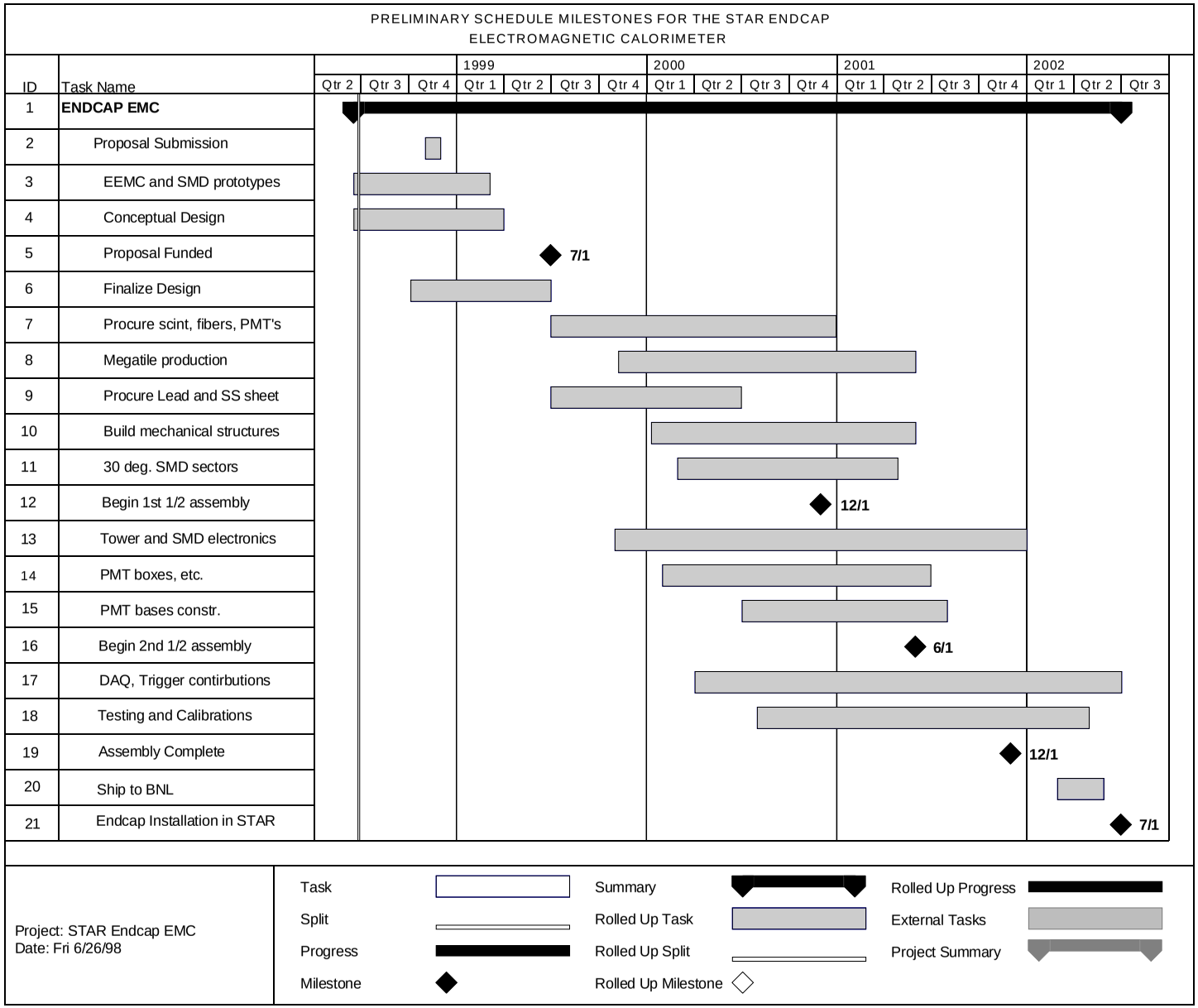

ID	Task Name
1	**ENDCAP EMC**
2	Proposal Submission
3	EEMC and SMD prototypes
4	Conceptual Design
5	Proposal Funded
6	Finalize Design
7	Procure scint, fibers, PMT's
8	Megatile production
9	Procure Lead and SS sheet
10	Build mechanical structures
11	30 deg. SMD sectors
12	Begin 1st 1/2 assembly
13	Tower and SMD electronics
14	PMT boxes, etc.
15	PMT bases constr.
16	Begin 2nd 1/2 assembly
17	DAQ, Trigger contirbutions
18	Testing and Calibrations
19	Assembly Complete
20	Ship to BNL
21	Endcap Installation in STAR

Project: STAR Endcap EMC
Date: Fri 6/26/98

Task
Split
Progress
Milestone
Summary
Rolled Up Task
Rolled Up Split
Rolled Up Milestone
Rolled Up Progress
External Tasks
Project Summary

References

[1] M.A. Shifman, A.I. Vainstein and V.I. Zakharov, Phys. Lett. B**78**, 443 (1978).

[2] J. Ashman *et al.*, Phys. Lett. B**206**, 364 (1988) and Nucl. Phys. B**328**, 1 (1990).

[3] D. Adams *et al.*, Phys. Rev. D**56**, 5330 (1997), and references therein.

[4] N. Isgur, in *Physics with Polarized Beams on Polarized Targets*, eds. J. Sowinski and S.E. Vigdor (World Scientific, Singapore, 1990) p. 252.

[5] For a recent review, see H.Y. Cheng, Int. J. Mod. Phys. A**11**, 5109 (1996).

[6] T. Gehrmann and W.J. Stirling, Phys. Rev. D**53**, 6100 (1996).

[7] L.E. Gordon and W. Vogelsang, Phys. Rev. D**48**, 3136 (1993).

[8] J. Huston *et al.*, Phys. Rev. D**51**, 6139 (1995).

[9] W. Vogelsang and A. Vogt, Nucl. Phys. B**453**, 334 (1995).

[10] J. Huston *et al.*, preprint hep-ph/9801444 (1998).

[11] C. Bourrely, J. Soffer, F.M. Renard and P. Taxil, Phys. Rep. **177**, 319 (1989).

[12] L.E. Gordon and W. Vogelsang, Phys. Rev. D**49**, 170 (1994).

[13] N. Hayashi, Y. Goto and N. Saito, in SPIN96 Proceedings, ed. C.W. de Jager *et al.* (World Scientific, Singapore, 1997), p. 349.

[14] M. Cacciari, M. Greco and P. Nason, preprint hep-ph/9803400 (1998), and references therein.

[15] G.K. Mallot *et al.*, in SPIN96 Proceedings, ed. C.W. de Jager *et al.* (World Scientific, Singapore, 1997), p. 441.

[16] D. Allasia *et al.*, Phys. Lett. B**258**, 493 (1991).

[17] J. Ashman *et al.*, Z. Phys. C**56**, 21 (1992).

[18] T.P. Cheng and L.-F. Li, Phys. Rev. Lett. **80**, 2789 (1998), and references therein.

[19] C. Bourrely and J. Soffer, Phys. Lett. B**314**, 132 (1993).

[20] M.A. Doncheski *et al.*, Phys. Rev. D**49**, 3261 (1994).

[21] C. Bourrely, J.Ph. Guillet and J. Soffer, Nucl. Phys. B**361**, 72 (1991).

[22] P. Taxil and J.M. Virey, Phys. Lett. B**364**, 181 (1995).

[23] J. Lopez and D. Nanopoulos, Phys. Rev. D**55**, 397 (1997).

[24] S.J. Brodsky and G.P. Lepage, Phys. Rev. D**22**, 2157 (1980) and Phys. Rev. D**24**, 2848 (1981).

[25] J. Ralston and D.E. Soper, Nucl. Phys. B**152**, 109 (1979).

[26] R.L. Jaffe, in Proc. 2nd Topical Workshop on Deep Inelastic Scattering off Polarized Targets, DESY, 1997 (preprint hep-ph/9710465), and references therein.

[27] R.L. Jaffe, Xuemin Jin and Jian Tang, Phys. Rev. Lett. **80**, 1166 (1998).

[28] X.-N. Wang and M. Gyulassy, Phys. Rev. Lett. **68**, 1480 (1992).

[29] A.H. Mueller and J.-W. Qiu, Nucl. Phys. B**268**, 427 (1986).

[30] E. Courant, in Proc. RHIC Spin Workshop, Brookhaven National Laboratory, April 1998.

[31] D. de Florian, M. Stratmann and W. Vogelsang, Phys. Rev. Lett. bf 81, 530 (1998).

[32] M. Burkardt and R.L. Jaffe, Phys. Rev. Lett. **70**, 2537 (1993).

[33] G. Apollinari, P. de Barbaro and M. Mishina, in Proc. 4th Intl. Conf. on Calorimetry in High Energy Physics, Elba, 1993; CDF II Technical Design Report, FNAL Pub-96/390-E, see
http://www-cdf.fnal.gov/upgrades/tdr/tdr_8_plug_cal.html.

[34] M. Adams *et al.*, Nucl. Instrum. Meth. A**378**, 131 (1996).

[35] S. Kim, Nucl. Instr. Meth. A**360**, 206 (1995).

[36] Final Design Report for Barrel EMC.

[37] W. Edwards, private communication.

[38] E. Bielick *et al.*, STAR Note 120 (1993).

[39] J. Straight, CDF internal report, 1993.

[40] S. Aota *et al.*, Nucl. Instr. Meth. A**357**, 71 (1995).

[41] B. Hübner, G.D. Westfall and A.M. Vander Molen, STAR Note 276 (1996).

[42] T. Sjöstrand, Comp. Phys. Commun. **82**, 74 (1994).

[43] W.B. Christie, STAR Note 169 (1995).

[44] STAR Note on Level 3 trigger.

[45] W.B. Christie and K. Shestermanov, STAR Note 196 (1995).

[46] M.E. Beddo, H. Spinka and D.G. Underwood, STAR Note 77 (1992).

[47] J. Alitti *et al.*, Phys. Lett. B**299**, 174 (1993).

[48] R. Brun *et al.*, GEANT User's Guide, CERN Program Library W5103.

[49] F. Abe *et al.*, Phys. Rev. D**48**, 2998 (1993).

[50] D.L. Adams *et al.*, Phys. Lett. B**264**, 462 (1991).

[51] D.L. Underwood, private communication.

[52] N. Akchurin *et al.*, Phys. Rev. D**48**, 3026 (1993); B.Z. Kopeliovich and L.I. Lapidus, Sov. J. Nucl. Phys. **19**, 114 (1974).

[53] M.A. Abolins *et al.*, Phys. Rev. Lett. **30**, 1183 (1973); E.L. Berger, A.C. Irving, and C. Sorensen, Phys. Rev. D**17**, 2971 (1978).

[54] D.L. Underwood, STAR Note 320 (1997).

[55] D.P. Grosnick *et al.*, Phys. Rev. D**55**, 1159 (1997).